Vascular phenotype identification and anti-angiogenic treatment recommendation: a pseudo-multiscale mathematical model of angiogenesis

L G Hutchinson [a], E A Gaffney [a], P K Maini [a], J Wagg [b], A Phipps [c], H M Byrne [d]

March 2, 2016

a. Wolfson Centre for Mathematical Biology, Mathematical Institute, University of Oxford, Andrew Wiles Building, Radcliffe Observatory Quarter, Woodstock Road, Oxford OX2 6GG, UK

b. Roche Pharmaceutical Research and Early Development, Clinical Pharmacology, Roche Innovation Centre Basel, Malzgasse 30, CH-4070 Basel, Switzerland

c. Pharma Research and Early Development, Roche Innovation Centre Welwyn, 6 Falcon Way, Shire Park, Welwyn Garden City, AL7 1TW, UK

d. Department of Computer Science, University of Oxford, Wolfson Building, Parks Road, Oxford OX1 3QD, UK

Corresponding author: Lucy Grace Hutchinson: hutchinson@maths.ox.ac.uk

Abstract

The development of anti-angiogenic drugs for cancer therapy has yielded some promising candidates, but novel approaches for interventions to angiogenesis have led to disappointing results. In addition, there is a shortage of biomarkers that are predictive of response to anti-angiogenic treatments. Consequently, the complex biochemical and physiological basis for tumour angiogenesis remains incompletely understood. We have adopted a mathematical approach to address these issues, formulating a spatially averaged multiscale model that couples the dynamics of VEGF, Ang1, Ang2 and PDGF, with those of mature and immature endothelial cells and pericyte cells. The model reproduces qualitative experimental results regarding pericyte coverage of vessels after treatment by anti-Ang2, anti-VEGF and combination anti-VEGF/anti-Ang2 antibodies. We used the steady state behaviours of the model to characterise angiogenic and non-angiogenic vascular phenotypes, and used mechanistic perturbations representing hypothetical anti-angiogenic treatments to generate testable hypotheses regarding transitions to non-angiogenic phenotypes that depend on the pre-treatment vascular phenotype. Additionally, we predicted a synergistic effect between anti-VEGF and anti-Ang2 treatments when applied to an immature pre-treatment vascular phenotype, but not when applied to a normalised angiogenic pre-treatment phenotype. Based on these findings, we conclude that changes in vascular phenotype are predicted to be useful as an experimental biomarker of response to treatment. Further, our analysis illustrates the potential value of non-spatial mathematical models for generating tractable predictions regarding the action of anti-angiogenic therapies.

Keywords: ordinary differential equation; linear stability; vessel normalisation.

1 Introduction

Angiogenesis is the process by which new blood vessels form from existing ones and, in the case of tumour angiogenesis, this results in the vascularization of a tumour. As such, it is an important therapeutic target in oncology. Anti-angiogenic cancer therapies were developed under the rationale that limiting the availability of essential resources to the tumour should reduce its rate of growth and spread (Folkman, 1971). However, the results of *in-vivo* non-clinical studies have shown that inhibition of pro-angiogenic factors can actually lead to increased blood flow and enhanced vessel normalisation, alongside vessel regression (Dickson et al., 2007, Fuxe et al., 2011, Han et al., 2009, Inai et al., 2004, Kienast et al., 2013, Lobov et al., 2002, Matsumoto et al., 2014, Thomas et al., 2013). It is clear, therefore, that the regulation of blood flow to tumours is more complex than was previously envisioned, and that therapeutic strategies could benefit from a deeper understanding of the processes involved in angiogenesis.

Observations of the first stages of vascular tumour development from Holash et al. (1999) show that for a rat glioma model, existing vessels are recruited to supply the tumour with oxygen and nutrients. The tumour grows around the recruited vessels which eventually regress, leading to tumour cell starvation and death. The release of angiogenic factors by hypoxic tumour cells stimulates the onset of angiogenesis. The hypoxic tumour cells produce Vascular Endothelial Growth Factor (VEGF) (other cells also produce smaller amounts of VEGF but these are neglected here), which binds to VEGFR-2 receptors expressed by endothelial cells (ECs) of nearby vessels, inducing EC proliferation and migration (Ferrara et al., 2003). Typically, newly formed tumour blood vessels surround the periphery of the tumour, and are tortuous and leaky, but the so-called normalisation of vessels (Jain, 2001), via maturation and coverage by smooth muscle cells, is essential for effective delivery of blood. A schematic of our interpretation of vessel maturation and normalisation is represented in Figure 1. The most well studied processes that drive normalisation involve the angiopoietin ligands and pericyte cells (PCs) (Goel et al., 2011). The ligands Ang1 and Ang2 compete for binding to Tie2 receptors expressed by ECs, and experimental work (Maisonpierre, 1997, Falcón et al., 2009, Thomas et al., 2013) has shown that Ang1 promotes maturation, whereas the antagonist Ang2 promotes de-maturation of vessels. Attachment of PCs to new vessels promotes their stability by plugging gaps in an otherwise leaky vasculature. In this study we account for

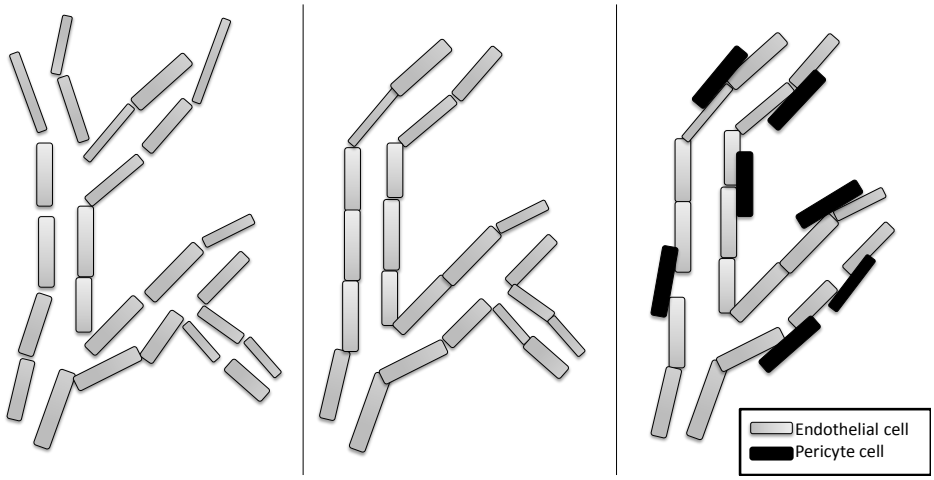

Figure 1: A schematic to illustrate our interpretation of immature, mature and normalised vessels. Left: tortuous, immature, leaky vessels with poor EC-EC adhesion and high branching. Centre: mature, less tortuous, less leaky vessels with good EC-EC adhesion. Right: normalised, mature vessels with good EC-EC adhesion and PC coverage to plug any gaps and support blood flow.

the important effects of vessel normalisation on the progression of angiogenesis.

Anti-angiogenic therapies are designed to reduce vessel density in order to inhibit the delivery of nutrients and oxygen to the tumour. The inhibition of angiogenesis through an array of molecular mechanisms continues in the non-clinical and clinical development space. Various growth factors, receptor tyrosine kinases and transcription factors have been investigated (Cook and Figg, 2010), either in monotherapy or in combination with chemotherapy (Weiss, 2004) or immunotherapy (Nishino et al., 2014). The first FDA approved anti-angiogenic drug was the anti-VEGF monoclonal antibody, bevacizumab (Avastin, Genentech), as an addition to chemotherapy for the treatment of metastatic colorectal cancer and non-small cell lung cancer, amongst others and as monotherapy in relapsed glioblastoma multiforme. Aflibercept (Zaltrap) inhibits the same target. Small molecule inhibitors of angiogenesis tend to hit multiple receptor targets. For example, Pazopanib (Votrient), approved for renal cell carcinoma, soft tissue sarcoma and gastrointestinal stromal tumours, targets multiple angiogenic receptors (VEGFR- 1,2,3, PDGFR, FGF, Kit, among others), (Du Bois et al., 2013). Sunitinib malate (Sutent, Pfizer) acts by inhibiting the activity of multiple tyrosine kinases, including the VEGFR2 and PDGFR-beta receptors (Goodman et al., 2007, Raymond et al., 2011, NCI, 2014).

Although many anti-angiogenic drugs hit multiple targets, to date, no added clinical benefit has arisen through combination of more than one anti-angiogenic drug. The reasons for efficacy in some cancer indications but not others are currently unknown,

although phenotypic differences in intra-tumoural vessel structure, cancer stage and individual patient characteristics have been postulated. In addition, the interplay between chemotherapy and anti-angiogenic drugs is not understood. Further confounding the ability to optimize treatment, no surrogate biomarkers of efficacy or diagnostic factors optimizing patients for anti-angiogenic therapy have been forthcoming, despite extensive research. Notwithstanding, from first principles, the concept of rationally targeting more than one target of angiogenesis appears valid. One area of interest is the inhibition of angiogenesis through angiopoietin perturbation. Ang-1 and Ang-2 are known to be drivers of angiogenesis although they appear to play conflicting roles between homeostasis and triggering angiogenesis. Drugs that target the angiopoietins have not yet been approved for use in humans. Trebaninib (Amgen), an inhibitor of Ang1 and Ang2 binding, showed a small increase in progression-free survival but failed to show an increase in overall survival for ovarian cancer patients when used in combination with chemotherapy (Monk et al., 2014). Further understanding of the interplay between different drivers of angiogenesis will surely aid improvements in therapy through rational drug design. Mathematical models of the pathways of angiogenesis will, likewise, enable researchers to optimize treatment regimens, by using models to simulate many permutations in treatment options and taking only the most promising to the clinic.

Experimental results have driven the design and development of mathematical and computational models of angiogenesis. Models can enhance our understanding of angiogenesis by integrating biological hypotheses that represent aspects of such a complex system (Zheng et al., 2013, Plank et al., 2004, Lignet et al., 2013, Billy et al., 2009), and for a review, see Scianna et al. (2013). From such models we gain insight into the expected influence of mechanistic model parameters, which relate to potential targets for therapy, on the overall morphology of developing vasculature (Zheng et al., 2013). In addition, mechanistic drug perturbations can be used to predict the effects of anti-angiogenic drugs as monotherapies and in combination with chemotherapy on vessel growth and morphology (Zheng et al., 2013, Lignet et al., 2013, Billy et al., 2009).

Two recent models in particular incorporate vessel normalisation as well as vessel density. Billy et al. (2009) present a pharmacologically driven, continuous, multiscale PDE model of angiogenesis and vascular tumour growth that accounts for the effects of the angiopoietins on the maturity of vasculature, and Zheng et al. (2013) present a one-dimensional, spatially resolved, continuous model that couples biochemical effects with

the biomechanical processes of PC attachment and one-dimensional vessel growth, and also takes into account vessel normalisation. Zheng et al. explicitly model the binding of ligands to their respective receptors and do not take tumour cells into account, whereas Billy et al. use a smooth, saturating function of ligand concentration to model the effects of angiogenic factors on EC proliferation and maturation, and couple their angiogenesis model to a tumour growth model. The model from Billy et al. predicts a theoretical threshold level of endostatin gene therapy below which treatment loses efficacy. Zheng et al. conclude from their simulations that combined anti-VEGF/anti-PDGF therapy has a superior anti-angiogenic effect compared to anti-VEGF therapy alone.

Mathematical models of angiogenesis, such as those described above, usually recommend anti-angiogenic treatment on a "one-size-fits-all" basis, rather than taking into account different behaviour regimes that the model may exhibit. A theoretical paper from Agur et al. (2003) investigates the conditions under which oscillations in tumour size occur in existing angiogenesis models in the absence of anti-angiogenic therapy, via analysis of Hopf bifurcations in the models. To our knowledge, none of the existing models of angiogenesis compare the effects of different anti-angiogenic drugs on vasculature with different phenotypic properties, such as well-normalised vessels versus immature, leaky vessels.

Our goal in this paper is to develop a mathematical model that can be used to categorize vessel phenotypes and to identify the effects of specific anti-angiogenic therapies that are suitable for treating each phenotype. In order to do this, we develop a complex mathematical model that includes details of the biochemistry involved in angiogenesis, and accounts for vessel density and normalisation. We take a similar approach to Zheng et al. for representing the biochemistry associated with neovascularisation, accounting for concentrations of free ligands and bound and unbound receptors explicitly. A reduced version of the model allows the analytical identification of four vessel phenotypes. Two phenotypes represent angiogenic behaviour, and two represent non-angiogenic behaviour. We perform simulations of the full model to investigate the interplay between anti-VEGF and anti-Ang2 therapies, demonstrating that a detailed mechanistic model built from biological hypotheses reproduces observed experimental results (Kienast et al., 2013). Motivated by experimental results from the same study, we also investigate whether synergistic effects are predicted for a bispecific anti-angiogenic antibody. We identify upstream parameters in the full model that represent potential drug targets that could effect transitions from

angiogenic to non-angiogenic phenotypes. We conclude that vessel phenotype (defined by the current steady state behaviour of the model variables) could be considered a useful biomarker for predicting response to novel anti-angiogenic treatments.

The remainder of this paper is organised as follows. In Section 2, we develop the full model and show examples of behaviours exhibited by the model. We proceed in Section 3 to analyse a simplified version of the full model in order to gain insight into possible long-term behaviour regimes. Section 4 contains the main results of our modelling: we begin by demonstrating that the long term behaviour of the full model is similar to that of the simplified model in Section 4.1, and we validate the qualitative behaviour of the full model using experimental results from Kienast et al. (2013) in Section 4.2.1, where we also predict the effects of the same anti-angiogenic treatments on an alternative pre-treatment vascular phenotype. We simulate perturbations to parameters that represent hypothetical drug treatments in Section 4.2.2, demonstrating that different pre-treatment vascular phenotypes require different perturbations for transition to a non-angiogenic phenotype.

2 Model development

Our model of angiogenesis comprises 16 time dependent, coupled, nonlinear ordinary differential equations (ODEs) that describe the evolution of ligands, receptors, ECs and PCs from the onset of angiogenesis. Units of concentration, μM, are used to represent four ligands, three receptor types and two cell types. We focus attention on a small, isolated region of approximately homogeneous tumour tissue (for example, 0.5mm^3 is a reasonable volume to consider, since it is on the scale of imaging data in Dobosz et al. (2014)). For simplicity, we neglect the dynamics of the tumour cells, and assume that the dynamics of its evolving vasculature are representative of the tumour as a whole. We assume there is no flux of ECs or PCs on the boundaries of the region represented. The terms density and concentration are used interchangeably when referring to cells. A schematic depicting all of the interactions that appear in the full model is shown in Figure 2.

The newly formed vessels in our model are described by the density of ECs, which are sub-divided into three distinct categories: mature ECs, immature ECs, and ECs with PC coverage (the maturity of ECs with PC coverage is not specified). We assume that immature ECs proliferate and die, produce Ang2 and PDGF, and express VEGFR2 and

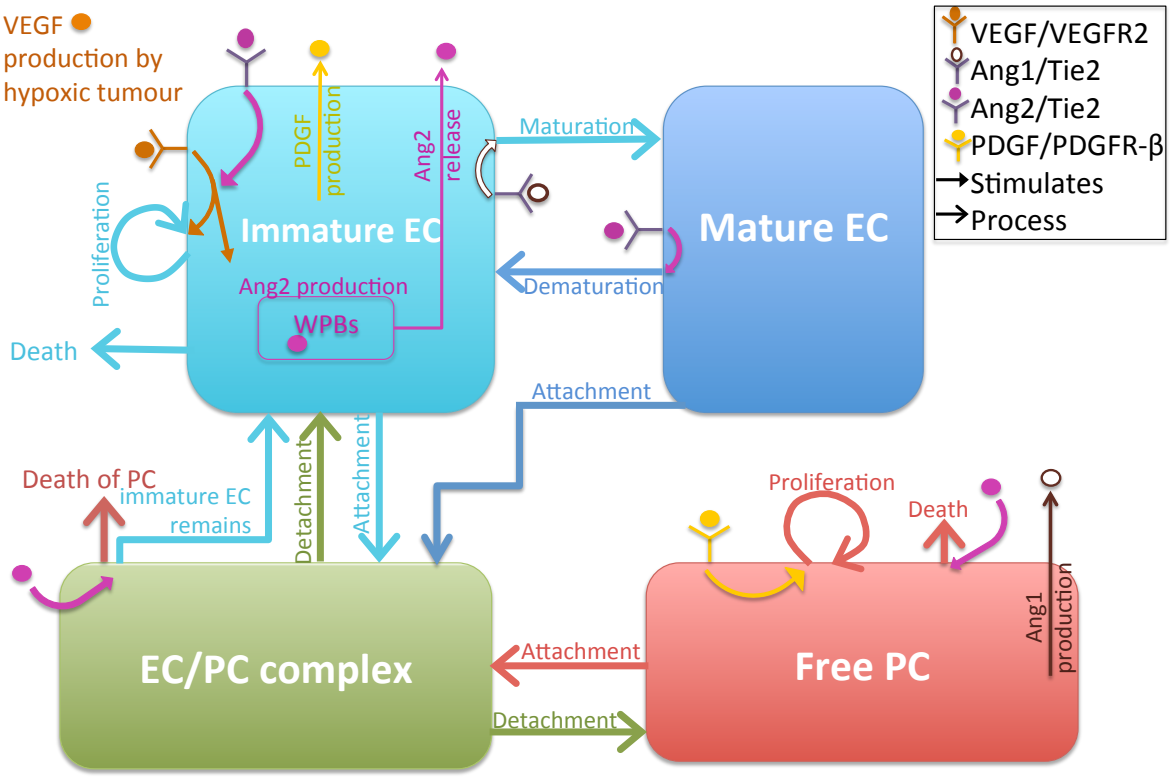

Figure 2: A schematic summarising the elements of angiogenesis incorporated into the full model. VEGF is produced in response to hypoxia in the tumour, and binds to VEGFR2 receptors expressed by ECs. Bound VEGF also increases the rate of production of Ang2 in Weibel Palade Bodies, from which it is released as the organelles become saturated. Immature ECs also produce PDGF at a constant rate, and die naturally via apoptosis. Ang2 competes with Ang1 for binding to the Tie2 receptor: an excess of bound Ang2 leads to de-maturation of ECs, and an excess of bound Ang1 leads to EC maturation. Ang2 binding also increases the proliferation rate of immature ECs. PDGF binds to PDGFR-β receptors expressed by PCs, upregulating PC proliferation. PCs die naturally and free Ang2 up-regulates PC death. PCs produce Ang1 and attach to both mature and immature ECs, forming the EC/PC complex that has no maturity rating, to increase the stability of vessels. PCs that are attached to ECs die naturally via apoptosis or due to high levels of extracellular Ang2, leaving behind a free EC which is automatically classed as immature.

Tie2 receptors (Falcón et al., 2009, Wang et al., 2002, Ferrara et al., 2003). Mature ECs and ECs with PC coverage also express VEGFR2 and Tie2 receptors, but do not proliferate, die or produce ligands in our model. We assume that immature ECs have loose EC-EC contacts and exhibit leakiness, whereas mature vessels have tight EC-EC contacts and are less leaky (Falcón et al., 2009, Goel et al., 2011). PC coverage plugs gaps between ECs, makes vessels more sturdy and enhances blood flow (although blood flow is beyond the scope of the current model) (Fuxe et al., 2011).

On the molecular scale, ligands are produced and bind to their respective receptors, and on the cellular scale, immature ECs and PCs proliferate. Since we model behaviour on two spatial scales, but do not include detailed spatial information, we describe our model as pseudo-multiscale. The biological mechanisms of synthesis and release of the ligands VEGF, Ang1, Ang2 and PDGF are taken into account in our model. As illustrated in Figure 2, VEGF binds to VEGFR2 receptors expressed by ECs and stimulates EC proliferation. Similarly, Ang1 and Ang2 compete for binding to the Tie2 receptor, and their combined downstream effect is to modulate the maturity of new vessels. Finally, PDGF binds to PDGFR-β receptors expressed by PCs and stimulates PC proliferation.

On the cellular scale, we assume that free PCs bind indiscriminately to mature and immature ECs. When PCs detach from ECs or the PC of an EC/PC complex dies, we assume an immature EC remains. We also assume that de-maturation occurs when the ratio of bound Ang2/bound Ang1 exceeds a given threshold, and maturation occurs otherwise. The dependence of maturity on the angiopoietins is based on experimental observations by Maisonpierre (1997). Table 1 summarises the dependent variables used in our model, as well as variable groupings that appear in the model equations.

2.1 Biochemical sub-models

In this subsection we present and explain the mathematical equations that describe the interactions included in the three sub-models that govern the biochemical aspects of our model.

2.1.1 VEGF sub-model

VEGF is produced by tumour cells in response to hypoxia. It binds VEGFR2 receptors expressed by ECs and is internalised, stimulating intracellular signals to upregulate EC

Variables and variable groupings			
Name	Description	Initial value	Unit
v	Free VEGF concentration	8×10^{-5}	μM
r_v	Total unbound VEGFR2 receptors	6×10^{-4}	μM
b_v	Total bound VEGFR2 receptors	6×10^{-4}	μM
a_1	Free Ang1	8×10^{-5}	μM
a_w	Total Ang2 stored in all WPBs	8×10^{-5}	μM
a_2	Free Ang2	8×10^{-5}	μM
r_a	Total unbound Tie2 receptors	6×10^{-4}	μM
b_{a_1}	Total bound Ang1/Tie2	3×10^{-4}	μM
b_{a_2}	Total bound Ang2/Tie2	3×10^{-4}	μM
p	PDGF-B	8×10^{-5}	μM
r_p	Total unbound PDGFR-β receptors	4×10^{-4}	μM
b_p	Total bound PDGFR-β receptors	4×10^{-4}	μM
E_i	Number density of immature ECs	4×10^{-9}	μM
E_m	Number density of mature ECs	8×10^{-9}	μM
P	Number density of free Pericytes	8×10^{-9}	μM
E_P	Number density of ECs with pericyte coverage	0	μM
E_T	$(E_i + E_m + E_P)$ Total endothelial cells	-	μM
P_T	$(P + E_P)$ Total pericyte cells	-	μM
v_b	$\left(\frac{s}{r+s}\right)$ Bound fraction of VEGFR2 receptors	-	none
a_b	$\left(\frac{b_{a_2}}{r_a+b_{a_1}+b_{a_2}}\right)$ Fraction of Tie2 receptors bound by Ang2	-	none
p_b	$\left(\frac{b_p}{r_p+b_p}\right)$Bound fraction of PDGFR-$\beta$ receptors	-	none

Table 1: Definitions of dependent variables and variable groupings in the full ODE model of angiogenesis, along with the default initial conditions used for numerical simulations.

proliferation. Although VEGF binding occurs via the process of dimerization, which is modelled explicitly in work from Jain et al. (2008), we exploit the results of stochastic models by Mac Gabhann et al. (2005) to motivate the use of a simpler one-to-one ligand-receptor binding model. Mac Gabhann et al. used experimental data to show that a one-to-one binding model was sufficient to model the VEGF/VEGFR2 receptor binding leading to activation of downstream signalling mechanisms. In more detail, we assume that free VEGF (v) binds reversibly to VEGFR2 receptors (r_v) to form VEGF/VEGFR2 complexes (b_v) via reactions of the form

$$\begin{aligned} v + r_v &\underset{k^v_{\text{off}}}{\overset{k^v_{\text{on}}}{\rightleftharpoons}} b_v, \\ b_v &\xrightarrow{k^v_{\text{int}}} \underset{product}{internal} + r_v, \end{aligned}$$

where k^v_{on} is the rate at which VEGF associates with VEGFR2 receptors to form a ligand/receptor complex, and k^v_{off} is the corresponding dissociation rate. We suppose that bound VEGF is internalised at rate k^v_{int}, and that this activates sub-cellular signalling pathways as the receptor is recycled to the cell surface. For simplicity, we assume instantaneous recycling of the VEGFR2 receptors, and that the "internal product" stimulates the onset of downstream signalling pathways.

Taking into consideration production, binding and decay, we assume that the evolution of extracellular VEGF concentration can be described by the following equation:

$$\text{Extracellular VEGF:} \quad \frac{\mathrm{d}v}{\mathrm{d}t} = \underbrace{D(E_m, E_P)}_{\text{VEGF production}} \overbrace{-k^v_{\text{on}}\, v\, r_v + k^v_{\text{off}}\, b_v}^{\substack{\text{VEGF association} \\ \text{and dissociation}}} \underbrace{- \delta_v\, v}_{\text{VEGF decay}}, \quad (1)$$

where δ_v is the basal natural decay rate of extracellular VEGF, and $D(E_m, E_P)$ represents the rate of VEGF production by tumour cells, although tumour cells are not explicitly included in this model. When defining $D(E_m, E_P)$, we assume that the rate at which VEGF is produced is a decreasing function of oxygen tension. Since we do not include a dependent variable for oxygen tension in this model, we introduce the term $D(E_m, E_P)$ as an indirect measure thereof. We assume that ECs that are mature (E_m) or have PC coverage (E_P) can transport oxygen, and that hypoxia is inversely proportional to the oxygen tension, since oxygen delivery reduces hypoxia in the tumour. We also assume that VEGF production increases with hypoxia. The functional form of the production

term is given by

$$D(E_m, E_P) = \frac{\alpha_v}{\frac{E_m+E_P}{E_0}+1},$$

where $(E_m + E_P)$ is the density of stable vessels, E_0 is the carrying capacity of ECs, and α_v is a constant to represent the maximal VEGF production rate. The production rate of VEGF by tumour cells decreases as the density of stable vessels increases, and when the stable vessel density is zero, VEGF is produced at a constant rate. We assume that the density of tumour cells remains fixed for the tumour region that we consider.

Throughout the model, we must account for the increase in receptor numbers (VEGFR2, Tie2, PDGFR-β) that occurs when cells (E_i, P) proliferate, and the reduction when cells die. For this, we assume that there is an average number of each type of receptor on each cell, basing our estimates for these receptor numbers on experimental work by Wang et al. (2002). In the absence of suitable experimental data to suggest otherwise, we assume that the average number of VEGFR2, Tie2 and PDGFR-β receptors per cell is the same, and denote by ϕ the average number of VEGFR2, Tie2 or PDGFR-β receptors per cell. Considering ligand binding and internalisation, and receptor generation and loss, the equations for unbound (r_v) and bound (b_v) VEGFR2 receptors are

$$\text{VEGFR2:} \quad \frac{\mathrm{d}r_v}{\mathrm{dt}} = \underbrace{-k^v_{\text{on}}\, v\, r_v + (k^v_{\text{off}} + k^v_{\text{int}})\, b_v}_{\substack{\text{VEGF association, dissociation} \\ \text{and internalisation}}} + \overbrace{\phi \times (\text{EC proliferation rate})}^{\text{receptor generation}} - \underbrace{\frac{r_v}{E_T}(\text{EC death rate})}_{\text{receptor loss}}, \tag{2}$$

$$\text{VEGF/VEGFR2 :} \quad \frac{\mathrm{d}b_v}{\mathrm{dt}} = \underbrace{k^v_{\text{on}} v\, r_v - (k^v_{\text{off}} + k^v_{\text{int}})\, b_v}_{\substack{\text{VEGF association, dissociation} \\ \text{and internalisation}}} - \underbrace{\frac{b_v}{E_T}(\text{EC death rate})}_{\text{receptor loss}}, \tag{3}$$

where E_T is the total EC density $(E_i + E_m + E_P)$ and the functional forms of the EC proliferation and death rates are below. Note that as ECs proliferate, only unbound receptors, r_v are produced, but both bound and unbound receptors, r_v and b_v, are lost as ECs die. The relation $\phi = \frac{r_v+b_v}{E_T}$ is used to derive the terms for receptor death in proportion to the relative concentrations of bound and unbound receptors.

Hill Functions: In our model, there are several instances of switch-like behaviour. The model is continuous in cell density, representing the behaviour of a large number of cells. Even though the switch in phenotype (or behaviour) of individual cells may happen very rapidly when a given threshold (of a ligand concentration, for example) is reached, this threshold may be cell specific and for a population of cells, distributed around the average threshold value. We capture this behaviour using second order Hill functions which we denote by

$$\mathrm{H}(a,b) = \frac{a^2}{a^2+b^2},$$

where a is a dependent variable and b is a threshold value, for instance. These functions give smooth switches between phenotypes and are more realistic than sharp switch functions when describing well mixed cell populations, and the order 2 is assumed a reasonable estimate.

2.1.2 Angiopoietins sub-model

The maturity of new vessels is controlled by the angiopoietins Ang1 and Ang2, which compete for binding to the Tie2 receptor expressed by ECs. In our model we account for Ang1 internalisation (Maisonpierre, 1997) and the synthesis of both ligands. Since Ang1 is produced by PCs, we assume that its production rate is linearly dependent on the PC density (Wakui et al., 2006, Fuxe et al., 2011). Ang2 is produced in sub-cellular organelles within ECs called Weibel Palade Bodies (WPBs) (Fiedler et al., 2004, Scharpfenecker et al., 2005), which we model explicitly. We assume that only immature ECs (E_i) produce Ang2, that there is a maximum concentration of intracellular Ang2 per cell which cannot be exceeded, and that Ang2 is produced at a rate which is upregulated in response to VEGF binding. We define the fractional occupancy of VEGFR2 receptors as v_b. In our model, as WPBs become saturated, Ang2 is rapidly released, and stored Ang2 is lost as ECs die. The total concentration of intracellular Ang2 across all ECs, a_w, is represented by the equation

$$\begin{aligned}\text{Intracellular Ang2}: \quad \frac{\mathrm{d}a_w}{\mathrm{dt}} &= \underbrace{\alpha_{a_w}(1+v_b)\left(\frac{A_0}{E_0}E_i - a_w\right)}_{\text{Ang2 production inside WPBs}} - \overbrace{\delta_{a_w}a_w}^{\text{decay}} \\ &\quad \underbrace{-\alpha_{a_2}\, a_w \mathrm{H}\left(a_w, \frac{A_0}{E_0}\frac{E_i}{2}\right)}_{\text{Ang2 exocytosis}} - \underbrace{\frac{a_w}{E_T}(\text{EC death rate})}_{\text{Ang2 loss as ECs die}}, \quad (4)\end{aligned}$$

where $\frac{A_0}{E_0}$ is the maximum amount of intracellular Ang2 per cell, v_b is the fraction of VEGFR2 receptors which are bound by VEGF, and $\alpha_{a_w}, \delta_{a_w}$ and α_{a_2} are constants representing the production, decay and release rates of Ang2, respectively. Since Ang2 is produced by immature ECs, its carrying capacity and exocytosis rate depend on the density of immature ECs, E_i: as E_i increases towards the EC carrying capacity, E_0 (see equation (13) later in this section), the maximum allowed intracellular Ang2 increases towards, A_0. We assume that in the absence of VEGF stimulation, immature ECs produce Ang2 at a base rate α_{a_w}, and that this rate is a linearly increasing function of bound VEGF, v_b. Ang2 exocytosis is modelled via a second order Hill function, where $\frac{A_0}{E_0}\frac{E_i}{2}$ is the concentration of intracellular Ang2 at which the release rate is half maximal. The functional form for the EC death rate is given below.

Extracellular Ang1, a_1, is produced by PCs that are free, P, or attached to ECs, E_P, $(P + E_P = P_T)$, and it binds Tie2 receptors, r_a, expressed by ECs to form the Ang1/Tie2 complex, b_{a_1}, and also decays naturally. Extracellular Ang2, a_2, is released by ECs as described above, and also binds to Tie2 receptors, r_a, to form the Ang2/Tie2 complex, b_{a_2}, and decays naturally. The evolution of the extracellular angiopoietins is modelled via the equations

$$\text{Extracellular Ang1:} \quad \frac{\mathrm{d}a_1}{\mathrm{dt}} = \underbrace{\alpha_{a_1}\, P_T}_{\text{Ang1 production}} - \overbrace{k^{a_1}_{\text{on}}\, a_1\, r_a + k^{a_1}_{\text{off}}\, b_{a_1}}^{\text{Ang1 association and dissociation}} - \underbrace{\delta_{a_1}\, a_1}_{\text{Ang1 decay}}, \tag{5}$$

$$\text{Extracellular Ang2:} \quad \frac{\mathrm{d}a_2}{\mathrm{dt}} = \underbrace{\alpha_{a_2}\, a_w \mathrm{H}\left(a_w, \frac{A_0}{E_0}\frac{E_i}{2}\right)}_{\text{Ang2 exocytosis}} - \overbrace{k^{a_2}_{\text{on}}\, a_2\, r_a + k^{a_2}_{\text{off}}\, b_{a_2}}^{\text{Ang2 association and dissociation}} - \underbrace{\delta_{a_2}\, a_2}_{\text{Ang2 decay}}. \tag{6}$$

In equation (5), α_{a_1} is the production rate of Ang1, the parameters representing the association and dissociation rates for Ang1/Tie2 binding are $k^{a_1}_{\text{on}}$ and $k^{a_1}_{\text{off}}$, respectively, and for Ang2/Tie2 association and dissociation, $k^{a_2}_{\text{on}}$ and $k^{a_2}_{\text{off}}$, respectively. The linear decay rates of Ang1 and Ang2 in the interstitium are represented by the parameters δ_{a_1} and δ_{a_2}, respectively.

As for the VEGF sub-model, we distinguish free and bound Tie2 receptors. Assuming as before that each cell has ϕ Tie2 receptors, we ensure that Tie2 receptors are generated as immature ECs (E_i) proliferate and lost as they die. The equations for Tie2 receptors,

r_a, Ang1/Tie2 complex, b_{a_1}, and Ang2/Tie2 complex, b_{a_2} are

$$\text{Tie2:}\quad \frac{\mathrm{d}r_a}{\mathrm{dt}} = \underbrace{-k_{\text{on}}^{a_1}\, a_1\, r_a + k_{\text{off}}^{a_1}\, b_{a_1}}_{\substack{\text{Ang1 association}\\ \text{and dissociation}}} \overbrace{-k_{\text{on}}^{a_2}\, a_2\, r_a + k_{\text{off}}^{a_2}\, b_{a_2}}^{\substack{\text{Ang2 association}\\ \text{and dissociation}}} + \underbrace{k_{\text{int}}^{a_1}\, b_{a_1}}_{\text{Ang1 internalisation}} + \underbrace{\phi \times (\text{EC proliferation rate})}_{\text{receptor generation}} - \underbrace{\frac{r_a}{E_T}(\text{EC death rate})}_{\text{receptor loss}}, \tag{7}$$

$$\text{Ang1/Tie2:}\quad \frac{\mathrm{d}b_{a_1}}{\mathrm{dt}} = \underbrace{k_{\text{on}}^{a_1}\, a_1\, r_a - k_{\text{off}}^{a_1}\, b_{a_1}}_{\substack{\text{Ang1 association}\\ \text{and dissociation}}} - \underbrace{k_{\text{int}}^{a_1}\, b_{a_1}}_{\text{Ang1 internalisation}} - \underbrace{\frac{b_{a_1}}{E_T}(\text{EC death rate})}_{\text{receptor loss}}, \tag{8}$$

$$\text{Ang2/Tie2:}\quad \frac{\mathrm{d}b_{a_2}}{\mathrm{dt}} = \underbrace{k_{\text{on}}^{a_2}\, a_2\, r_a - k_{\text{off}}^{a_2}\, b_{a_2}}_{\substack{\text{Ang2 association}\\ \text{and dissociation}}} - \overbrace{\frac{b_{a_2}}{E_T}(\text{EC death rate})}^{\text{receptor loss}}, \tag{9}$$

where $k_{\text{int}}^{a_1}$ is the internalisation rate of Ang1, and as Ang1 is internalised, we assume that receptors are recycled to the cell surface similarly to the VEGFR2 receptor in equations (2)-(3).

2.1.3 PDGF sub-model

In our model, PDGF, p, is produced by immature ECs, E_i, and binds to the PDGFR-β receptor, r_p, expressed by PCs, to form the PDGF/PDGFR$-\beta$ complex, b_p. The binding process may be represented by

$$p + r_p \underset{k_{\text{off}}^p}{\overset{k_{\text{on}}^p}{\rightleftharpoons}} b_p,$$

where k_{on}^p denotes the association rate of PDGF to PDGFR-β and k_{off}^p denotes the corresponding dissociation rate. Combining the above processes, we deduce that the evolution of free PDGF may be described by the following ODE:

$$\text{Free PDGF:}\quad \frac{\mathrm{d}p}{\mathrm{dt}} = \underbrace{\alpha_p\, E_i}_{\substack{\text{PDGF production}\\ \text{by immature ECs}}} \overbrace{-k_{\text{on}}^p\, p\, r_p + k_{\text{off}}^p\, b_p}^{\substack{\text{PDGF association}\\ \text{and dissociation}}} - \underbrace{\delta_p\, p}_{\text{PDGF decay}} \tag{10}$$

where α_p is the assumed constant rate at which immature ECs produce PDGF, and δ_p is its natural decay rate.

Similarly to the VEGF and angiopoietins sub-models described above, we assume that receptors are generated as cells (in this case PCs) proliferate and lost as they die. Assuming ϕ receptors per PC, we model the free and bound PDGFR-β receptors by the equations

$$\text{PDGFR-}\beta\text{:} \qquad \frac{\mathrm{d}r_p}{\mathrm{dt}} = \overbrace{-k^p_{\text{on}}\ p\ r_p + k^p_{\text{off}}\ b_p}^{\substack{\text{PDGF association}\\ \text{and dissociation}}} + \underbrace{\phi \times (\text{PC proliferation rate})}_{\text{receptor generation}} - \underbrace{\frac{r_p}{P_T}(\text{PC death rate})}_{\text{receptor loss}}; \tag{11}$$

$$\text{PDGF/PDGFR-}\beta\text{:} \qquad \frac{\mathrm{d}b_p}{\mathrm{dt}} = \underbrace{k^p_{\text{on}}\ p\ r_p - k^p_{\text{off}}\ b_p}_{\substack{\text{PDGF association}\\ \text{and dissociation}}} - \underbrace{\frac{b_p}{P_T}(\text{PC death rate})}_{\text{receptor loss}}; \tag{12}$$

where we assume that free receptors are produced as PCs proliferate, and both free and bound receptors are lost as PCs die. The total density of PCs is the sum of free PCs and PCs attached to ECs, $P_T = P + E_P$. The functional forms of the terms for PC proliferation and death are described below.

2.2 Cell dynamics sub-model

In our model we consider two types of cells: ECs and PCs. We subdivide the ECs into three categories for immature ECs (E_i), mature ECs (E_m) and ECs with PC coverage (E_P) and denote by P the concentration of free PCs. Before presenting the ODEs governing the evolution of E_i, E_m, E_P and P, we pause to describe briefly the processes included in the cell dynamics sub-model.

We assume that ECs undergo three processes: proliferation, death and attachment to PCs. Similarly, we assume that PCs proliferate, die and attach to ECs. PCs are assumed to bind to mature and immature ECs at the same rate, ζ. By contrast and for simplicity, we suppose that when PCs detach, the ECs to which they were bound become immature, regardless of their previous status. The attachment and detachment of PCs to ECs can

be represented by the following reactions:

$$\begin{aligned} E_m + P &\xrightarrow{\zeta} E_P, \\ E_i + P &\xrightarrow{\zeta} E_P, \\ E_P &\xrightarrow{\nu} E_i + P, \\ E_P &\xrightarrow{\epsilon} E_i. \end{aligned}$$

where ϵ is the PC death rate. We assume that when PCs attached to ECs die, the unattached ECs are immature.

In our model, the proliferation of immature ECs is stimulated by VEGF binding and upregulated by Ang2 binding, and the death of immature ECs occurs when there is insufficient bound VEGF for proliferation. Similarly, we assume that the proliferation of free PCs is stimulated by PDGF binding. According to experimental data, PCs die when there is a high local concentration of extracellular Ang2 (Park et al., 2014), and we take this into account when we model the death of PCs, assuming supression of PCs via extracellular Ang2 applies to free and attached PCs. For simplicity we assume that the death rate is the same for free PCs and PCs attached to ECs.

2.2.1 Endothelial cells

We assume that the dominant processes regulating the concentration of immature ECs, E_i, are proliferation, death, and attachment and detachment of PCs. Using the law of mass action to represent the attachment and detachment of PCs to ECs, and including exchange terms between mature and immature ECs, the equation for the evolution of immature ECs takes the form

$$\begin{aligned} \text{Immature ECs:} \quad \frac{\mathrm{d}E_i}{\mathrm{dt}} = & \underbrace{\theta\, \mathrm{H}\left(v_b, c_{ep}\right)\left(1 + \mathrm{H}(a_b, c_a)\right)\left(1 - \frac{E_T}{E_0}\right) E_i}_{\text{EC proliferation}} - \underbrace{\rho\, \mathrm{H}\left(c_d, v_b\right) E_i}_{\text{EC death}} \\ & \underbrace{-\zeta\ P E_i + \nu\ E_P}_{\substack{\text{association and dissociation} \\ \text{of PCs with ECs}}} + \underbrace{\epsilon\left(\frac{a_2}{A_0} + \mathrm{H}(c_{ep}, p_b)\right) E_P}_{\substack{\text{PC death due} \\ \text{to high Ang2 levels} \\ \text{or low PDGF levels}}} \\ & \underbrace{-\eta\ \mathrm{H}\left(\lambda, \frac{b_{a_2}}{b_{a_1}}\right) E_i}_{\text{maturity increase}} + \underbrace{\mu\ \mathrm{H}\left(\frac{b_{a_2}}{b_{a_1}}, \lambda\right) E_m}_{\text{maturity decrease}}. \end{aligned} \tag{13}$$

In equation (13), the parameter θ represents the half-maximal proliferation rate of immature ECs and ρ represents the maximum death rate of immature ECs. In our model, EC proliferation is switched on (via a second order Hill function), when the fractional occupancy of VEGFR2 receptors, v_b, reaches the threshold, c_{ep}, and a logistic growth of immature ECs is assumed. Experimental observations from Lobov et al. (2002) suggest that EC proliferation in the presence of VEGF is enhanced by Ang2 binding. Therefore, in our model, the proliferation rate of immature ECs is upregulated (via an additional second order Hill function) when the fraction of Tie2 receptors bound by Ang2, a_b, reaches another threshold, c_a. We assume that EC death is switched on (via a second order Hill function) when the concentration of bound VEGFR2 receptors falls below a threshold, c_d. As mentioned above, PCs attach to ECs at rate ζ and detach at rate ν. Further, when attached PCs die, the remaining EC is assumed to be immature. The attachment and detachment of PCs are represented in the third and fourth bracketed terms in equation (13). We assume that vessel maturity is determined by the proportions of bound Ang1 and bound Ang2. In equation (13), we assume that both the increase and decrease in maturity take the form of second order Hill functions, and these are given by the fifth and sixth bracketed terms in equation (13), where η and μ are constants that represent the maximum de-maturation and maturation rates, and λ is the ratio of bound Ang2/bound Ang1 above which ECs tend to transition to an immature phenotype.

Receptor generation and loss terms in equations (2), (3), (4) and (7)-(9), refer to the rates of immature EC proliferation and death. From equation (13) we deduce that the functional forms for these terms are

$$\text{(EC proliferation rate)} = \theta \, \mathrm{H}\left(v_b, c_{ep}\right)\left(1 + \mathrm{H}\left(a_b, c_a\right)\right)\left(1 - \frac{E_T}{E_0}\right) E_i,$$

and

$$\text{(EC death rate)} = \rho \, \mathrm{H}\left(c_d, v_b\right) E_i.$$

In our model, mature ECs do not proliferate or die, and PCs are assumed to attach to mature and immature ECs at the same rate. Combining these effects we deduce that the

equation governing the evolution of the mature ECs is

$$\text{Mature ECs:}\quad \frac{\mathrm{d}E_m}{\mathrm{dt}} = \underbrace{-\zeta\ P\ E_m}_{\substack{\text{association of PCs}\\ \text{with ECs}}} + \underbrace{\eta\ \mathrm{H}\left(\lambda, \frac{b_{a_2}}{b_{a_1}}\right)\ E_i}_{\text{maturity increase}} \underbrace{-\mu\ \mathrm{H}\left(\frac{b_{a_2}}{b_{a_1}}, \lambda\right)\ E_m}_{\text{maturity decrease}}. \tag{14}$$

2.2.2 Pericyte cells

We suppose that the processes dominating the time evolution of free PCs are proliferation, death and attachment to ECs. Combining these processes yields the following ODE:

$$\text{Free pericytes:}\quad \frac{\mathrm{d}P}{\mathrm{dt}} = \underbrace{\kappa\ \mathrm{H}(p_b, c_{pp})\left(1 - \frac{P_T}{P_0}\right)P}_{\text{PC proliferation}} \underbrace{-\ \epsilon\ \left(\frac{a_2}{A_0} + \mathrm{H}(c_{pp}, p_b)\right)\ P}_{\substack{\text{PC death due}\\ \text{to high Ang2 levels}\\ \text{or low PDGF levels}}} \underbrace{-\ \zeta\ P\ (E_i + E_m)\ +\ \nu\ E_P}_{\substack{\text{association and dissociation}\\ \text{of PCs with ECs}}}. \tag{15}$$

In equation (15), κ is the maximum proliferation rate of PCs, ϵ scales the PC death rate and P_0 is the carrying capacity of PCs. We assume a logistic growth of PCs, where PCs compete for space with one another but not with ECs. Experimental observations from Armulik et al. (2005) suggest that fractional PC coverage in normal vessels ranges from 10%-50%. In our model, therefore, we assume that the maximum carrying capacity of PCs, P_0, is half that of ECs, E_0. We assume that PC proliferation is switched on (via a second order Hill function) when the fractional occupancy of PDGFR-β receptors, p_b, reaches the threshold for proliferation, c_{pp}. In our model, PC death is controlled by the fractional occupancy of PDGFR-β and the presence of extracellular Ang2. When the proportion of bound PDGF/PDGFR-β falls below the threshold, c_{ep}, or when Ang2 levels are high (compared to the reference concentration, A_0) the PC death rate increases.

2.2.3 Endothelial cell/pericyte complex

We assume that the adhesion of PCs to both mature and immature ECs can be modelled via a simple binding reaction, which is represented by the law of mass action. In our model, ECs with PC coverage are quiescent, they therefore do not proliferate or die, and are neither classed as mature nor immature. Taking into account the association

and dissociation of PCs to ECs, and the death of PCs due to a high extracellular Ang2 concentration, we represent the EC/PC complex, E_P, by the equation

$$\text{EC/PC complex:} \qquad \frac{\mathrm{d}E_P}{\mathrm{dt}} = \underbrace{\zeta\ P\ (E_i + E_m) - \nu\ E_P}_{\substack{\text{association and dissociation} \\ \text{of PCs with ECs}}} \underbrace{- \epsilon\ \left(\frac{a_2}{A_0} + \mathrm{H}(c_{pp}, p_b)\right)\ E_P}_{\substack{\text{PC death due} \\ \text{to high Ang2 levels} \\ \text{or low PDGF levels}}}. \tag{16}$$

We assume that PCs bound to ECs die at the same rate as free PCs and that the ECs to which they were attached are immature.

In equations (11) and (12), PDGFR-β receptor generation and loss depend on the proliferation and death rates of PCs. Combining equations (15) and (16), the evolution of the total PC density, $P_T = P + E_P$, satisfies

$$\frac{\mathrm{d}P_T}{\mathrm{dt}} = \kappa\ \mathrm{H}(p_b, c_{pp}) \left(1 - \frac{P_T}{P_0}\right)\ P - \epsilon \left(\frac{a_2}{A_0} + \mathrm{H}(c_{pp}, p_b)\right)\ P_T.$$

Further we have that

$$\text{(PC proliferation rate)} = \kappa\ \mathrm{H}(p_b, c_{pp}) \left(1 - \frac{P_T}{P_0}\right)\ P,$$

and

$$\text{(PC death rate)} = \ \epsilon\ \left(\frac{a_2}{A_0} + \mathrm{H}(c_{pp}, p_b)\right)\ P_T.$$

These expressions are used in equations (11) and (12) to determine the rate at which PDGFR-β receptors are created and lost from the system.

2.3 Model summary

Our model comprises sixteen time dependent ODEs. Each ODE describes how levels of a particular physical variable evolve over time. Twelve of these equations represent biochemical interactions between ligands and receptors, and four represent the dynamics of mature and immature ECs, and free and bound PCs. The full set of equations is listed

below for completeness.

Free VEGF:
$$\frac{\mathrm{d}v}{\mathrm{dt}} = \frac{\alpha_v}{\frac{E_m+E_P}{E_0}+1} - k^v_{\mathrm{on}}\ v\ r_v + k^v_{\mathrm{off}}\ b_v - \delta_v\ v, \tag{1}$$

VEGFR2:
$$\begin{aligned}\frac{\mathrm{d}r_v}{\mathrm{dt}} = &-k^v_{\mathrm{on}}\ v\ r_v + (k^v_{\mathrm{off}} + k^v_{\mathrm{int}})\ b_v \\ &+\phi\ \theta\ \mathrm{H}\left(v_b, c_{ep}\right)\left(1+\mathrm{H}(a_b, c_a)\right)\left(1-\frac{E_T}{E_0}\right)\ E_i \\ &-\rho\ \mathrm{H}(c_d, v_b)\frac{E_i}{E_T}\ r_v,\end{aligned} \tag{2}$$

VEGF/VEGFR2:
$$\frac{\mathrm{d}b_v}{\mathrm{dt}} = k^v_{\mathrm{on}}\ v\ r_v - (k^v_{\mathrm{off}} + k^v_{\mathrm{int}})\ b_v - \rho\ \mathrm{H}(c_d, v_b)\frac{E_i}{E_T}\ b_v, \tag{3}$$

Free Ang1:
$$\frac{\mathrm{d}a_1}{\mathrm{dt}} = \alpha_{a_1}\ P_T - k^{a_1}_{\mathrm{on}}\ a_1\ r_a + k^{a_1}_{\mathrm{off}}\ b_{a_1} - \delta_{a_1}\ a_1, \tag{4}$$

Intracellular Ang2:
$$\begin{aligned}\frac{\mathrm{d}a_w}{\mathrm{dt}} = &\alpha_{a_w}\ (1+v_b)\left(\frac{A_0}{E_0}E_i - a_w\right) - \delta_{a_w}\ a_w \\ &-\alpha_{a_2}\ a_w\ \mathrm{H}\left(a_w, \frac{E_i}{E_0}\frac{A_0}{2}\right) - \rho\ \mathrm{H}\left(c_d, v_b\right)\frac{E_i}{E_T}\ a_w,\end{aligned} \tag{5}$$

Free Ang2:
$$\begin{aligned}\frac{\mathrm{d}a_2}{\mathrm{dt}} = &\alpha_{a_2}\ a_w\ \mathrm{H}\left(a_w, \frac{A_0}{E_0}\frac{E_i}{2}\right) - k^{a_2}_{\mathrm{on}}\ a_2\ r_a + k^{a_2}_{\mathrm{off}}\ b_{a_2} \\ &-\delta_{a_2}\ a_2,\end{aligned} \tag{6}$$

Tie2:
$$\begin{aligned}\frac{\mathrm{d}r_a}{\mathrm{dt}} = &-k^{a_1}_{\mathrm{on}}\ a_1\ r_a + (k^{a_1}_{\mathrm{off}} + k^{a_1}_{\mathrm{int}})\ b_{a_1} - k^{a_2}_{\mathrm{on}}\ a_2\ r_a + k^{a_2}_{\mathrm{off}}\ b_{a_2} \\ &+\phi\ \theta\ \mathrm{H}\left(v_b, c_{ep}\right)\left(1+\mathrm{H}(a_b, c_w)\right)\left(1-\frac{E_T}{E_0}\right)\ E_i \\ &-\rho\ \mathrm{H}\left(c_d, v_b\right)\frac{E_i}{E_T}\ r_a,\end{aligned} \tag{7}$$

Ang1/Tie2:
$$\frac{\mathrm{d}b_{a_1}}{\mathrm{dt}} = k^{a_1}_{\mathrm{on}}\ a_1\ r_a - (k^{a_1}_{\mathrm{off}} + k^{a_1}_{\mathrm{int}})\ b_{a_1} - \rho\ \mathrm{H}\left(c_d, v_b\right)\frac{E_i}{E_T}\ b_{a_1}, \tag{8}$$

Ang2/Tie2:
$$\frac{\mathrm{d}b_{a_2}}{\mathrm{dt}} = k^{a_2}_{\mathrm{on}}\ a_2\ r_a - k^{a_2}_{\mathrm{off}}\ b_{a_2} - \rho\ \mathrm{H}\left(c_d, v_b\right)\frac{E_i}{E_T}\ b_{a_2}, \tag{9}$$

Free PDGF:
$$\frac{\mathrm{d}p}{\mathrm{dt}} = \alpha_p\ E_i - k^p_{\mathrm{on}}\ p\ r_p + k^p_{\mathrm{off}}\ b_p - \delta_p\ p, \tag{10}$$

PDGFR-β:
$$\frac{\mathrm{d}r_p}{\mathrm{dt}} = -k^p_{\mathrm{on}}\ p\ r_p + k^p_{\mathrm{off}}\ b_p + \phi\ \kappa\ \mathrm{H}(p_b, c_{pp}) \left(1 - \frac{P_T}{P_0}\right)\ P$$
$$-\epsilon\ \left(\frac{a_2}{A_0} + \mathrm{H}(c_{pp}, p_b)\right)\ r_p, \tag{11}$$

PDGF/PDGFR-β:
$$\frac{\mathrm{d}b_p}{\mathrm{dt}} = k^p_{\mathrm{on}}\ p\ r_p - k^p_{\mathrm{off}}\ b_p - \epsilon\ \left(\frac{a_2}{A_0} + \mathrm{H}(c_{pp}, p_b)\right)\ b_p, \tag{12}$$

Immature ECs:
$$\frac{\mathrm{d}E_i}{\mathrm{dt}} = \theta\ \mathrm{H}\left(v_b, c_{ep}\right)\left(1 + \mathrm{H}(a_b, c_a)\right)\left(1 - \frac{E_T}{E_0}\right)\ E_i - \rho\ \mathrm{H}\left(c_d, v_b\right)\ E_i$$
$$-\zeta\ P\ E_i + \nu\ E_P + \epsilon\ \left(\frac{a_2}{A_0} + \mathrm{H}(c_{pp}, p_b)\right)\ E_P$$
$$-\eta\ \mathrm{H}\left(\lambda, \frac{b_{a_2}}{b_{a_1}}\right)\ E_i + \mu\ \mathrm{H}\left(\frac{b_{a_2}}{b_{a_1}}, \lambda\right)\ E_m, \tag{13}$$

Mature ECs:
$$\frac{\mathrm{d}E_m}{\mathrm{dt}} = -\zeta\ P\ E_m + \eta\ \mathrm{H}\left(\lambda, \frac{b_{a_2}}{b_{a_1}}\right)\ E_i - \mu\ \mathrm{H}\left(\frac{b_{a_2}}{b_{a_1}}, \lambda\right)\ E_m, \tag{14}$$

Free pericytes:
$$\frac{\mathrm{d}P}{\mathrm{dt}} = \kappa\ \mathrm{H}(p_b, c_{pp}) \left(1 - \frac{P_T}{P_0}\right)\ P - \epsilon\ \left(\frac{a_2}{A_0} + \mathrm{H}(c_{pp}, p_b)\right)\ P$$
$$-\zeta\ P\ (E_i + E_m) + \nu\ E_P, \tag{15}$$

EC/PC complex:
$$\frac{\mathrm{d}E_P}{\mathrm{dt}} = \zeta\ P\ (E_i + E_m) - \nu\ E_P - \epsilon\ \left(\frac{a_2}{A_0} + \mathrm{H}(c_{pp}, p_b)\right)\ E_P, \tag{16}$$

where all variables and grouped variables are defined in Table 1.

Parameter values for the full model were obtained via an extensive search of the biological literature. Of the 39 parameters, 22 were estimated from the literature. Where no appropriate data were available, parameters were typically estimated from values of parameters in similar systems, or from existing mathematical models. Otherwise, parameters were estimated based on their qualitative effects on model behaviour. The default parameter values used in model simulations are listed in Table C1.

2.4 Numerical simulations of the full model

We simulate the full model with initial conditions that represent the onset of angiogenesis. We assume that ECs ($E_i + E_m + E_P$) have a density that is $\frac{3}{20}$ of their carrying capacity, that all PCs are free (no PC coverage) and that $\frac{2}{3}$ of ECs are mature. The initial conditions for all variables are given in Table 1. Figure 3 shows two typical simulations of the full model, and from these simulations, it is clear that there are multiple long-term behaviour

regimes of the full model. In the next section, we turn to a simplified version of the full model in order to explore analytically the possible long term behaviour regimes.

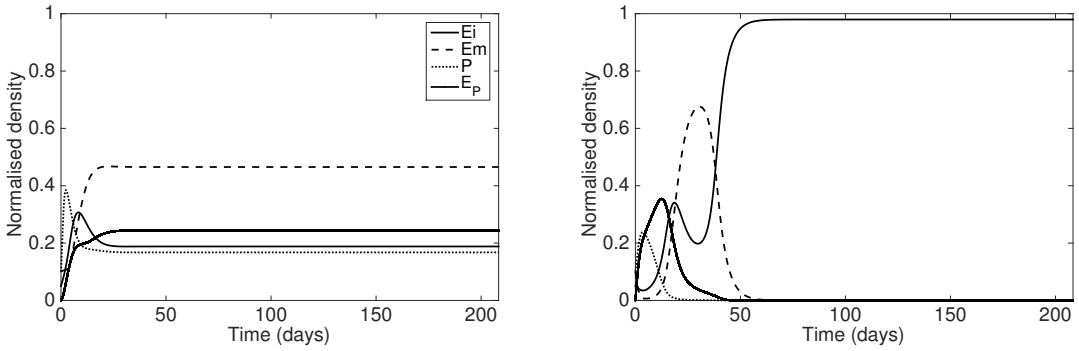

Figure 3: Numerical simulations of the full model equations (1)-(16) using parameter values from Table C1 (except $\zeta = 0.24$ in (b)) and initial conditions from Table 1.

3 Cell dynamics sub-model analysis results

In this section we analyse a decoupled version of the cell dynamics sub-model in order to gain insight into the possible long-term behaviour regimes of the full model. The results are used to identify possible vascular phenotypes, and furthermore to recommend specific anti-angiogenic treatments to suit them.

The simplified model is obtained from the full model by ignoring the dependence on VEGF, Ang1, Ang2 and PDGF of the proliferation and death rates of ECs and PCs, and the maturation and de-maturation rates of ECs, and treating them as constants. Under these assumptions, equations (13)-(16) reduce to give:

Immature ECs:
$$\frac{\mathrm{d}E_i}{\mathrm{dt}} = \hat{\theta}\left(1 - \frac{E_i + E_m + E_P}{E_0}\right) E_i - \hat{\rho}\, E_i - \zeta\, P\, E_i + \nu\, E_P + \hat{\epsilon}\, E_P - \hat{\eta}\, E_i + \hat{\mu}\, E_m, \tag{17}$$

Mature ECs:
$$\frac{\mathrm{d}E_m}{\mathrm{dt}} = -\zeta\, P\, E_m + \hat{\eta}\, E_i - \hat{\mu}\, E_m, \tag{18}$$

Free pericytes:
$$\frac{\mathrm{d}P}{\mathrm{dt}} = \hat{\kappa}\left(1 - \frac{P + E_P}{P_0}\right) P - \hat{\epsilon}\, P - \zeta\, P\, (E_i + E_m) + \nu\, E_P, \tag{19}$$

EC/PC complex:
$$\frac{\mathrm{d}E_P}{\mathrm{dt}} = \zeta\, P\, (E_i + E_m) - \nu\, E_P - \hat{\epsilon}\, E_P, \tag{20}$$

wherein the constants $\hat{\theta}, \hat{\rho}, \hat{\kappa}, \hat{\epsilon}, \hat{\eta}$ and $\hat{\mu}$ have replaced the functional forms in the full model:

$$\theta\ \mathrm{H}\left(v_b, c_{ep}\right)\left(1+\mathrm{H}(a_b, c_a)\right) \rightarrow \hat{\theta}; \qquad \rho\ \mathrm{H}\left(c_d, v_b\right) \rightarrow \hat{\rho}; \qquad \kappa\ \mathrm{H}(p_b, c_{pp}) \rightarrow \hat{\kappa};$$

$$\epsilon\ \left(\frac{a_2}{A_0}+\mathrm{H}(c_{pp}, p_b)\right) \rightarrow \hat{\epsilon}; \qquad \eta\ \mathrm{H}\left(\lambda, \frac{b_{a_2}}{b_{a_1}}\right) \rightarrow \hat{\eta}; \qquad \mu\ \mathrm{H}\left(\frac{b_{a_2}}{b_{a_1}}, \lambda\right) \rightarrow \hat{\mu}.$$

3.1 Steady state solutions

By setting time derivatives to zero in equations (17)-(20), we identify five steady state solutions, including two vessel-free solutions for which $E_i = E_m = E_P = 0$. In another steady solution, only ECs lacking PC coverage are present ($E_P = P = 0, E_i, E_m > 0$). For the final two steady solutions, all cell types coexist. The solutions for which one or more of E_i, E_m, P, E_P are zero can be written as follows:

$$\begin{array}{llllll}
\text{(i)} & E_i = 0; & E_m = 0; & P = 0; & E_P = 0; \\
\text{(ii)} & E_i = 0; & E_m = 0; & P = P_0\left(1-\dfrac{\hat{\epsilon}}{\hat{\kappa}}\right); & E_P = 0; \\
\text{(iii)} & E_i = \dfrac{E_0\left(1-\frac{\hat{\rho}}{\hat{\theta}}\right)}{\left(1+\frac{\hat{\eta}}{\hat{\mu}}\right)}; & E_m = \dfrac{E_0\left(1-\frac{\hat{\rho}}{\hat{\theta}}\right)}{\left(1+\frac{\hat{\mu}}{\hat{\eta}}\right)}; & P = 0; & E_P = 0.
\end{array}$$

Solution (i) represents the trivial non-angiogenic phenotype. It exists and is biologically realistic in the positive quadrant of parameter space and corresponds to tumour sub-regions where the conditions are such that angiogenesis does not take place. Solution (ii) corresponds to an alternative non-angiogenic steady state in which only free PCs are non-zero. This solution exists and is physically realistic in regions of parameter space for which $\frac{\hat{\epsilon}}{\hat{\kappa}} \leq 1$, ie the death rate of PCs is smaller than the proliferation rate of PCs. Steady state (iii) is characterised by the coexistence of mature and immature ECs; this corresponds to a highly angiogenic vascular phenotype with no PC normalisation. The balance between mature and immature ECs in this steady state depends on the parameters $\hat{\eta}$ and $\hat{\mu}$, which are coupled to the concentrations of bound Ang1 and bound Ang2 in the full model. Specifically, for $\hat{\eta} > \hat{\mu},\ E_m > E_i$ and vice-versa. The third steady state exists as a physically realistic solution when $\frac{\hat{\rho}}{\hat{\theta}} \leq 1$, ie the proliferation rate of immature ECs is greater than the death rate of immature ECs.

For the fourth and fifth steady states, all cell types have non-zero densities and the

corresponding values of P, denoted P_+ and P_-, are the roots of the quadratic

$$P^2 + \left[\left(E_0\left(1-\frac{\hat{\rho}}{\hat{\theta}}\right) - P_0\left(1-\frac{\hat{\epsilon}}{\hat{\kappa}}\right)\right) + \frac{(\nu+\hat{\epsilon})}{\zeta}\right] P \qquad (21)$$
$$+P_0\left[\frac{\hat{\epsilon}}{\hat{\kappa}}E_0\left(1-\frac{\hat{\rho}}{\hat{\theta}}\right) - \left(1-\frac{\hat{\epsilon}}{\hat{\kappa}}\right)\frac{(\nu+\hat{\epsilon})}{\zeta}\right] = 0.$$

The remaining steady states are known functions of P_+ and P_-:

$$\text{(iv)} \quad E_i = \frac{E_0(1-\frac{\hat{\rho}}{\hat{\theta}})(\nu+\hat{\epsilon})(\zeta P_+ + \hat{\mu})}{(\nu+\hat{\epsilon}+\zeta P_+)(\hat{\eta}+\hat{\mu}+\zeta P_+)}, \qquad E_m = \frac{\hat{\eta}E_i}{\zeta P_+ + \hat{\mu}},$$

$$P = P_+, \qquad E_P = \frac{\zeta\left(1-\frac{\hat{\rho}}{\hat{\theta}}\right)P_+}{\nu+\hat{\epsilon}+\zeta P_+},$$

$$\text{(v)} \quad E_i = \frac{E_0(1-\frac{\hat{\rho}}{\hat{\theta}})(\nu+\hat{\epsilon})(\zeta P_- + \hat{\mu})}{(\nu+\hat{\epsilon}+\zeta P_-)(\hat{\eta}+\hat{\mu}+\zeta P_-)}, \qquad E_m = \frac{\hat{\eta}E_i}{\zeta P_- + \hat{\mu}},$$

$$P = P_-, \qquad E_P = \frac{\zeta\left(1-\frac{\hat{\rho}}{\hat{\theta}}\right)P_-}{\nu+\hat{\epsilon}+\zeta P_-}.$$

Analysis of steady states (iv) and (v) (see Appendix A) reveals that (v) is never biologically feasible in the current parameter regime defined in Table 2, and that the region in which solution (iv) is biologically realistic is where

$$\left(\frac{\hat{\kappa}}{\hat{\epsilon}} - 1\right)(\nu+\hat{\epsilon}) > \zeta E_0\left(1-\frac{\hat{\rho}}{\hat{\theta}}\right) > 0. \qquad (22)$$

Parameter	Normalised value(s)	Units
$\hat{\rho}$	[0.001 0.08] (0.02)	h^{-1}
$\hat{\epsilon}$	[0.01 0.08] (0.02)	h^{-1}
$\hat{\eta}$	0.01	h^{-1}
$\hat{\mu}$	0.01	h^{-1}
$\hat{\theta}$	0.04	h^{-1}
$\hat{\kappa}$	0.04	h^{-1}
ζ	0.1	h^{-1}
ν	0.05	h^{-1}
E_0	1	dimensionless
P_0	0.5	dimensionless

Table 2: Normalised parameter values for analysis of the uncoupled cell dynamics sub-model. The default values for $\hat{\rho}$ and $\hat{\epsilon}$ are given in round brackets. The ranges of values used to generate Figure 4 are given in square brackets. See Table C1 for original sources of parameters.

A linear stability analysis for each of the steady states (i)-(iv) is detailed in Appendix

B. In Figure 4 we summarise the results of our steady state and linear stability analyses by showing where in $\left(\frac{\hat{\rho}}{\hat{\theta}}, \frac{\hat{\epsilon}}{\hat{\kappa}}\right)$ parameter space each of solutions (i)-(iv) is physically realistic, and is linearly stable.

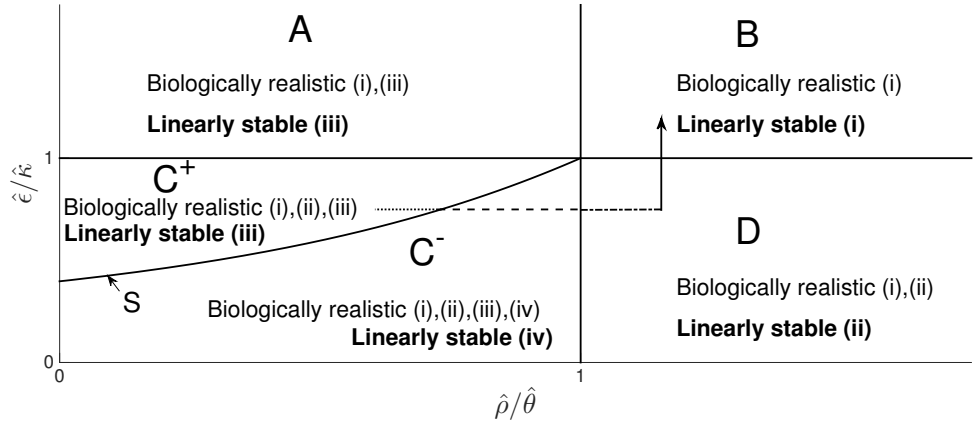

Figure 4: Diagram summarising how the existence and linear stability of steady states (i)-(iv) depend on parameters $\frac{\hat{\rho}}{\hat{\theta}}$ and $\frac{\hat{\epsilon}}{\hat{\kappa}}$. Biological feasibility was determined analytically by identifying regions where $E_i, E_m, P, E_P \geq 0$ and linear stability was determined from the signs of the real parts of the eigenvalues of the Jacobian, J, evaluated at the steady states. Parameter values are listed in Table 2. Region C is sub-divided into two regions by the curve S on which $\left(\frac{\hat{\kappa}}{\hat{\epsilon}} - 1\right)(\nu + \hat{\epsilon}) = \zeta E_0 \left(1 - \frac{\hat{\rho}}{\hat{\theta}}\right)$. Below S, solution (iv) is feasible and locally stable; above S, solution (iv) is unfeasible and solution (iii) is linearly stable. See equation (22) for details. The arrow shows an example of a path in $\left(\frac{\hat{\rho}}{\hat{\theta}}, \frac{\hat{\epsilon}}{\hat{\kappa}}\right)$ space to transition from an angiogenic to a non-angiogenic phenotype, and details are given in the text.

Our analysis has shown that the cell dynamics sub-model from equations (17)-(20) does not exhibit bistability in the current parameter regime (see Figure 4). The transitions between regions defined in Figure 4 are of biological interest. They indicate how, when treating an angiogenic tumour which has sections exhibiting angiogenic phenotype (iii) or (iv), the ratios of $\frac{\hat{\rho}}{\hat{\theta}}$ and $\frac{\hat{\epsilon}}{\hat{\kappa}}$ can be modulated to switch to a non-angiogenic phenotype such as (i) or (ii).

An example of a path in $\left(\frac{\hat{\rho}}{\hat{\theta}}, \frac{\hat{\epsilon}}{\hat{\kappa}}\right)$ space that could lead from an angiogenic phenotype to a non-angiogenic phenotype is shown by the arrow in Figure 4, which starts in region C^+, where (iii) is linearly stable, and passes through regions C^-, D and ends in B, where the trivial non-angiogenic solution (i) is linearly stable. In region C^+, steady states (i) and (ii) are biologically feasible, but unstable. The real parts of the eigenvalues of the Jacobian evaluated at (iii) are all negative in region C^+, but for increasing $\frac{\hat{\rho}}{\hat{\theta}}$ and fixed $\frac{\hat{\epsilon}}{\hat{\kappa}}$, the real part of one of the eigenvalues of the Jacobian becomes positive, so (iii) is no longer linearly stable after the curve S defined by inequality (22) is crossed (see Appendix

B for details). In addition, as S is crossed from left to right, the solutions for (iv) become biologically feasible (see Appendix A) and also linearly stable, and all cell types coexist in this region. Continuing to increase $\frac{\hat{\rho}}{\hat{\theta}}$ at fixed $\frac{\hat{\epsilon}}{\hat{\kappa}}$, the concentrations of E_i, E_m and E_P decrease until they all become zero at $\frac{\hat{\rho}}{\hat{\theta}} = 1$. At this point, solution (iv) reduces to solution (ii). In region D, the real parts of the eigenvalues of the Jacobian evaluated at (ii) are negative. Now increasing $\frac{\hat{\epsilon}}{\hat{\kappa}}$ for some fixed value of $\frac{\hat{\rho}}{\hat{\theta}} > 1$, steady state (ii) reduces to steady state (i) when $\frac{\hat{\epsilon}}{\hat{\kappa}} = 1$, and in region B, the trivial, non-angiogenic steady state solution (i) is linearly stable.

The concentrations of the cell types within the stable steady states are shown as a two dimensional colour plot in Figure 5. These plots indicate that there are no discontinuities at the boundaries between parameter regions. In the next section, cell density plots will be directly compared with others generated from the full model.

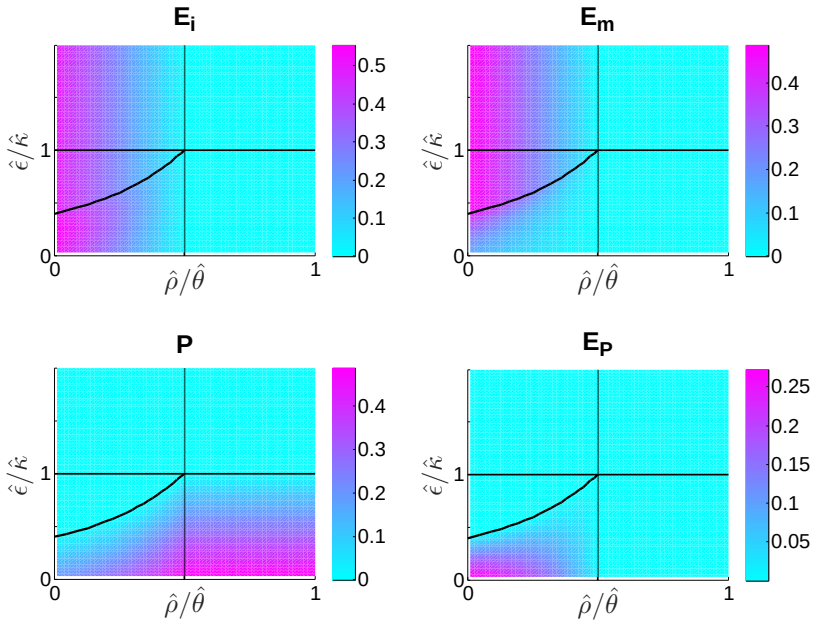

Figure 5: Plots to show the solutions for E_i, E_m, P and F for steady states (i)-(iv). Parameter values are listed in Table 2. The boundary of the region of feasibility of (iv) is shown by a thick black line and arises from inequality (22).

Summary of linear stability analysis

- There are four biologically feasible ($E_i, E_m, P, E_P \geq 0$) steady state solutions to the simplified cell dynamics sub-model in the current parameter regime. One additional

solution is not feasible in the current parameter regime but is feasible in other parameter regimes (see Appendix A for details).

- The feasibility and stability of each of the steady state solutions depend on the ratios $\frac{\hat{\rho}}{\hat{\theta}}$ and $\frac{\hat{\epsilon}}{\hat{\kappa}}$.
- There are no regions of bistability in the current parameter regime, and all steady states are linearly stable in exactly one region of the positive quadrant of $\left(\frac{\hat{\rho}}{\hat{\theta}}, \frac{\hat{\epsilon}}{\hat{\kappa}}\right)$ space.

4 Full model results

In this section we revert to the full model, identifying conditions under which its behaviour is the same as that of the simpler one. We use experimental data to validate the model qualitatively, and make predictions about the impact of administering existing anti-angiogenic therapies to an alternative pre-treatment phenotype. Finally, we demonstrate how the full model can be used for phenotype-specific anti-angiogenic drug target identification.

4.1 Corroboration of steady state results

The simplified model gives an insight into the possible long term behaviours of cell densities when coupling to the subcellular biochemistry is neglected. In this subsection we show that the behaviour regimes identified for the simple model are relevant to the behaviour of the full model.

To compare the stable steady states of the full model with those of the simplified model, equations (1)-(16) were solved for values of θ and κ that span several orders of magnitude (with the values of all other parameters including ϵ and ρ held fixed), and results are shown in Figure 6. We assume that equations (1)-(16) have reached a steady state when the time derivative of the full system is less than $10^{-5}h^{-1}$.

Comparison of Figures 5 and 6 reveals several common features and several discrepancies. Some similarities between the steady state behaviour of the full model shown in Figure 6 and the simplified model shown in Figure 5 are as follows: parameter space defined by the EC proliferation rate, θ, and the PC proliferation rate, κ, is divided into distinct regions where different steady states are linearly stable; there is a region of parameter space in which free and bound PCs are non-zero and the bounding region is

qualitatively similar for Figures 5 and 6; immature EC density attains its maximum for large θ and small κ; mature and immature ECs reach higher densities in the steady state for large θ; free PCs have a higher density for small θ and the EC/PC complex has a larger density for large θ.

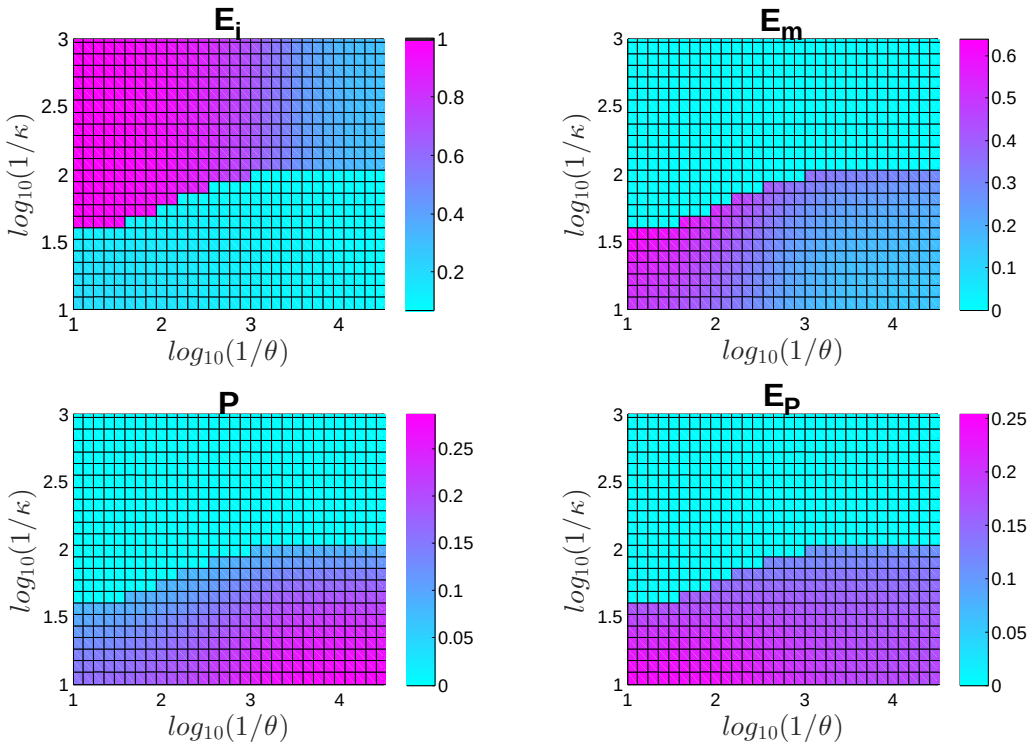

Figure 6: Steady state solutions for E_i, E_m, P and F using the full model (equations(1)-(16)) for values of $10^{-4.5} \leq \theta \leq 10^{-1}$ and $10^{-3} \leq \kappa \leq 10^{-1}$ and with all other parameters taken from Table C1.

The most notable discrepancy between Figures 5 and 6 is that $E_m \ll E_i$ for low κ (where no PCs are present), and $E_i \ll E_m$ for high κ (where PCs are present) in Figure 6, whereas in Figure 5 for low $\frac{\hat{\rho}}{\hat{\theta}}$ and low $\frac{\hat{\epsilon}}{\hat{\kappa}}$, immature ECs and PCs coexist at similar densities. The lack of immature ECs in regions with high PC concentration in the stable steady states of the full model can be explained in terms of the upstream biochemical interactions of Ang1 and Ang2. Where it exists, steady state (iii) of the simplified model takes the form $E_m = \frac{\hat{\eta}}{\hat{\mu}} E_i$, ie the ratio of immature to mature vessels is the ratio of the de-maturation to maturation functions. For the full model, PCs produce the growth factor Ang1 that is needed for maturation, and Ang2 is produced by immature ECs and leads to further de-maturation (a positive feedback loop for Ang2 induced de-

maturation). Consequently, in the case $P_T = 0$, μ H $\left(\frac{b_{a_2}}{b_{a_1}}, \lambda\right) \gg \eta$ H $\left(\lambda, \frac{b_{a_2}}{b_{a_1}}\right)$ which leads to $E_i \gg E_m$, and where $P_T \neq 0$, η H $\left(\lambda, \frac{b_{a_2}}{b_{a_1}}\right) \gg \mu$ H $\left(\frac{b_{a_2}}{b_{a_1}}, \lambda\right)$, which leads to $E_m \gg E_i$, and therefore to steady states where one EC type becomes predominant. In addition to these observations, it appears from Figure 6 that a very low value of θ would be required to observe steady states (i) and (ii) in the previous section. In the following subsections, we validate our model qualitatively using published experimental data, then go on to identify biochemical parameters associated with interventions that could achieve a transition from an angiogenic to a non-angiogenic steady state.

4.2 Anti-angiogenic therapies

The application of anti-angiogenic drugs to tumours has revealed that many candidate drugs act by normalising vessels and stimulating vessel regression (Goel et al., 2011). While the anti-tumour benefit of normalised vessels remains unclear, it has been suggested that they aid the delivery of chemotherapeutic agents, or improve the oxygen delivery, reducing hypoxia-induced VEGF production (Jain, 2005). Consequently, an alternative goal of anti-angiogenic therapy is to improve vessel normalisation while decreasing vessel density. In the context of the phenotypes identified for our model, this corresponds to a post-therapy phenotype (iv) with high normalisation.

The simplified and full models can be used to identify paths in parameter space that lead to a transition from the basin of attraction of a highly angiogenic steady state (for example, solutions (iii) and (iv)), to an alternative steady state solution (such as (i) or (iv) characterised by a high degree of vessel normalisation). Highly angiogenic vascular networks are associated with poor clinical outcome, where less dense, normalised networks are associated with a positive clinical outcome (see Table 1 in Jain (2005) for a summary). It has also been suggested that the promotion of vessel growth in addition to normalisation, alongside the administration of chemotherapy, could lead to a positive clinical outcome due to the enhanced ability of vasculature to deliver cytotoxic molecules, and this case corresponds to solution (iv) characterised by a high vessel density and high normalisation (Rivera and Bergers, 2015, Wong et al., 2015).

In the following sections, we simulate the effects of anti-VEGF, anti-Ang2 and a combined anti-VEGF/anti-Ang2 antibody on vessels of two alternative pre-treatment phenotypes, then we investigate transitions from highly angiogenic, (iii), or normalised angiogenic, (iv), pre-treatment phenotypes to non angiogenic (i) or highly normalised (iv)

end-points.

4.2.1 Anti-VEGF and anti-Ang2 antibodies

In this section, we perform a qualitative validation of the full model against experimental data.

In experiments described in Kienast et al. (2013), KPL-4 tumour-bearing mice were treated with either an anti-VEGF antibody, an anti-Ang2 antibody, a bispecific anti-VEGF/anti-Ang2 antibody (Crossmab) or a control treatment after the mean tumour volume for each group reached 150mm^3. The number of vessels per mm^3 of viable tumour tissue and the PC coverage of vessels were quantified by histology at the end of the study (day 63). Animals treated with anti-VEGF or Crossmab treatment had lower vessel densities than the control group on average, but the result was not statistically significant ($p > 0.05$) due to large variability and a small sample size. PC coverage was greater in all treatment groups compared to the control group, and treatment with Crossmab resulted in a statistically significant ($p < 0.05$) increase in PC coverage compared to anti-VEGF treatment, anti-Ang2 treatment and the control group. The experimental results are superimposed onto our simulated results in Figure 7.

Since PCs were present for all experimental groups, we focus on the coexistence pre-treatment phenotype. Now anti-VEGF antibodies are known to neutralise free VEGF, while anti-Ang2 antibodies neutralise free Ang2 and Crossmab neutralises both ligands (Kienast et al., 2013). We simulate anti-VEGF therapy by increasing the VEGF clearance rate, δ_v, and anti-Ang2 therapy by increasing the Ang2 clearance rate, δ_{a_2}. Crossmab is simulated by increasing both clearance rates simultaneously. In the absence of sufficiently detailed experimental data, we are unable to fully parameterise our model. Consequently, we do not claim that our model is able to generate quantitative results, although we can validate its qualitative predictions against the observations of Kienast et al..

Using the default steady state (iv) concentrations for all variables of the full model as initial conditions, anti-VEGF and anti-Ang2 therapies were simulated for a range of values of δ_v and δ_{a_2}. The results presented in Figure 7 show that anti-VEGF treatment leads to a decrease in vessel density and an increase in PC coverage, in line with experimental results. Increasing the rate of Ang2 clearance also leads to an increase in PC coverage in the steady state, but the effect of anti-Ang2 therapy on PC coverage saturates when p exceeds the value at which all extracellular Ang2 is neutralised. While simulations show

that the addition of anti-Ang2 therapy to anti-VEGF therapy is not predicted to decrease the total EC density, (see Figure 7a), it does increase PC coverage (see Figure 7b).

In conclusion, the full model produces results in qualitative agreement with experimental data for PC coverage following anti-angiogenic treatment. Although experimental results showed a decrease in vessel density following Crossmab therapy compared to anti-VEGF therapy alone, the result was not statistically significant. In our simulations, we found that Crossmab therapy did not lead to a larger decrease in EC density compared to anti-VEGF therapy. The same mechanistic, drug specific, perturbations could not have been performed using the simplified model due to lack of biochemical detail, justifying the need for a fully coupled model of angiogenesis.

Immature pre-treatment phenotype

We use the full model to predict the impact of anti-VEGF, anti-Ang2 and combined treatments on an immature vessel network. Figure 8 shows the stable ($E_m + E_P$) and immature (E_i) cell densities after initiation of anti-VEGF, anti-Ang2 and Crossmab treatments. Simulation of anti-VEGF treatment results in a decrease in immature vessel density, but no switch from the immature vessel phenotype. Simulation of anti-Ang2 treatment leads to an initial "lag" period, during which there is a small reduction in immature EC density, followed by a switch to a normalised phenotype approximately 100 days post treatment. Close inspection of the cell densities and biochemical variables during this lag period (data not shown) reveals that for anti-Ang2 treatment, PCs (which have a very low, but non-zero density) begin to proliferate since there is less free Ang2 to supress them; the PCs produce Ang1, which binds to Tie2 receptors, eventually reaching a concentration that activates the maturation switch. Since there are now fewer immature ECs producing Ang2, the suppression of PCs remains low, allowing their rapid growth. Decreasing the threshold ratio of $\frac{\text{bound Ang2}}{\text{bound Ang1}}$ for maturation delays the switch from an immature to a mature phenotype (data not shown) which supports this explanation.

Anti-VEGF and anti-Ang2 monotherapy simulations resulted in decreases in total EC density of 11% and 10% respectively, and Crossmab therapy resulted in a decrease in total EC density of 41% for the immature pre-treatment phenotype. Since the decrease in EC density after Crossmab therapy is greater than the sum of the decreases resulting from individual therapies, the effect can be described as synergistic for the example shown.

Our model simulations predict that the switch to a normalised phenotype, with PC

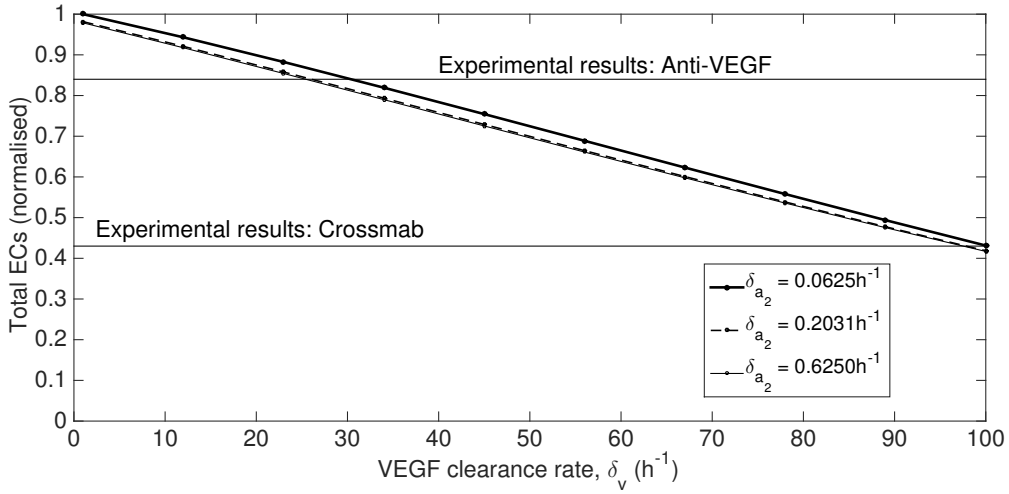

(a)

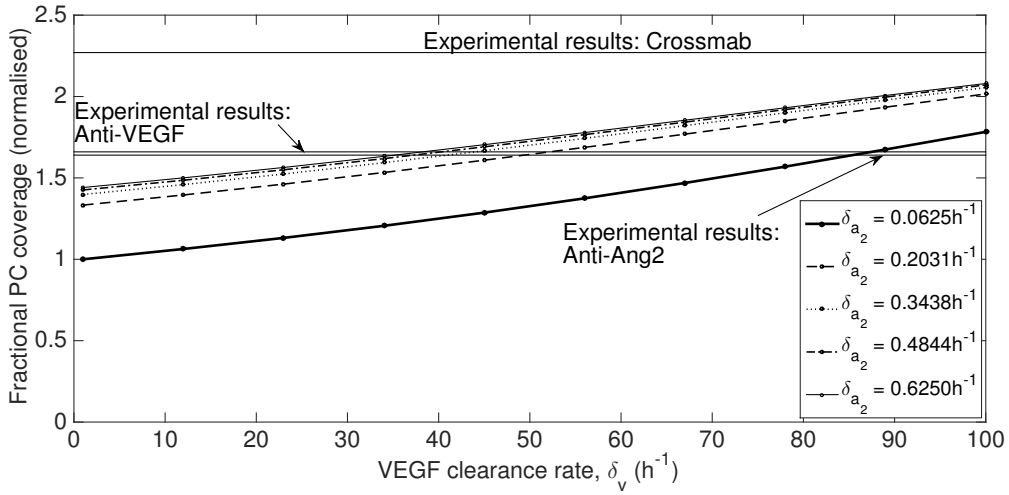

(b)

Figure 7: Numerical results for EC density ($E_i + E_m + E_P$) and PC coverage ($E_P/(E_i + E_m + E_P)$) in the steady state using equations (1) - (16) with the default parameter set given in Table C1 and $1h^{-1} \leq \delta_v \leq 100h^{-1}$ and $0.0625h^{-1} \leq \delta_{a_2} \leq 0.625h^{-1}$. The control values for δ_v and δ_{a_2} are $1h^{-1}$ and $0.0625h^{-1}$ respectively. Initial conditions were the steady state densities of all variables with no treatment and results were normalised to the total EC density or PC coverage with no treatment. Parameter scans for anti-VEGF, and combined anti-VEGF/anti-Ang2 treatments show that simulations suggest that anti-VEGF and Crossmab treatments reduce EC density compared to no treatment and anti-VEGF, anti-Ang2 and Crossmab treatment increase fractional PC coverage compared to no treatment. Experimental results (Kienast et al., 2013) for the decrease in EC density and increase in PC coverage (normalised to control) for all treatments, except where anti-Ang2 therapy, which did not result in EC density different from the control, are shown as horizontal lines for comparison with our simulated results. The decrease in EC density in the experimental results for Crossmab therapy was not statistically significant compared to anti-VEGF therapy.

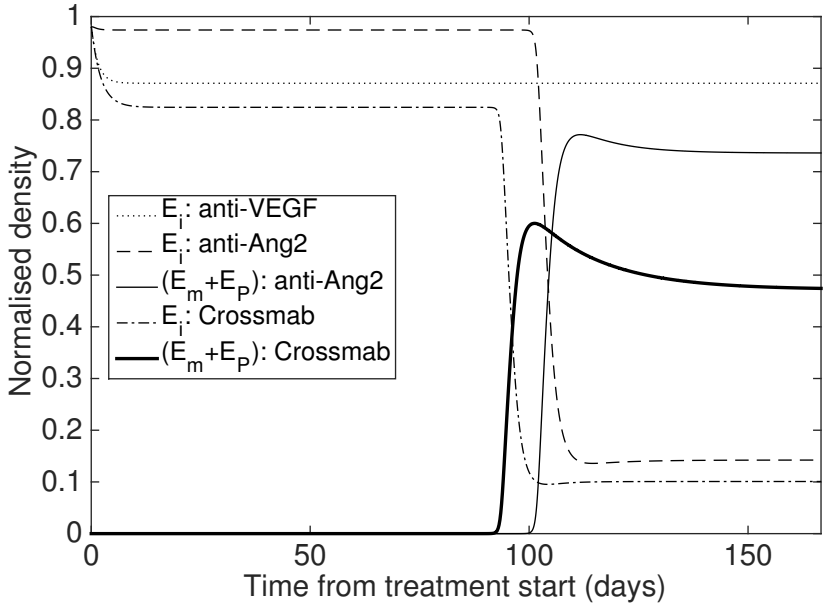

Figure 8: Simulation of anti-VEGF, anti-Ang2 and Crossmab, treatment for an immature pre-treatment phenotype shows that anti-VEGF treatment alone leads to a small decrease in immature vessel density, but anti-Ang2 and Crossmab treatment lead to a switch to the normalised phenotype after a delay of around 100 days. The immature pre-treatment phenotype is defined by the steady state densities of all variables with $\delta_{a_2} = 0.02h^{-1}$ and all other parameters taken from Table C1. For anti-VEGF treatment, $\delta_v = 60h^{-1}$ and for anti-Ang2 treatment $\delta_{a_2} = 0.4h^{-1}$, for Crossmab treatment $\delta_v = 60h^{-1}$ and $\delta_{a_2} = 0.4h^{-1}$ and treatment begins at day 0. $E_m + E_P$ for anti-VEGF treatment is zero for the length of the simulation and therefore is not shown.

coverage, occurs after administration of either anti-Ang2 or Crossmab therapies. The fractional PC coverage increases after simulations of anti-Ang2 therapy and Crossmab therapy, but not anti-VEGF therapy.

4.2.2 Phenotype-specific treatment recommendations

In this subsection we identify parameters in the full model that could be varied to effect a transition from an angiogenic to a non-angiogenic phenotype. The grouped parameters $\hat{\theta}, \hat{\rho}, \hat{\kappa}$ and $\hat{\epsilon}$ that appear in the simplified model are coupled to upstream biochemical processes in the full model, and the biochemical parameters may be perturbed to effect the desired transition from one basin of attraction to another.

The EC proliferation rate depends on the fractional occupancy of VEGFR2 receptors in the full model. Perturbations to parameters that control VEGF production, binding or decay should aid a transition from a stable coexistence steady state to a stable steady state where E_i and E_m are small, (ie from the left to the right side of Figure 6). Similarly, since the total proliferation rate of PCs depends on the fractional occupancy of PDGFR-β receptors, perturbations to parameters that control PDGF production, binding and decay should aid a transition from the coexistence steady state (iv) to a steady state of lower PC density, ie from bottom to top of Figure 6. For a normalised angiogenic pre-treatment phenotype, we perturb VEGF and PDGF related parameters simultaneously to approach the least angiogenic phenotype (i).

Figure 9 shows the results of simultaneous perturbations to VEGF and PDGF associated parameters for a normalised pre-treatment phenotype steady state (iv). A transition from the coexistence steady state to an immature steady state with a low EC density can be achieved by decreasing the VEGF production rate, α_v, and perturbing one of the PDGF associated parameters α_p, k^p_{on} or δ_p.

For the "runaway angiogenesis" highly immature pre-treatment phenotype (iii) where $E_i \gg E_m$ and $P, E_P \approx 0$, we decrease VEGF associated parameters with an aim to decrease E_T, moving from the upper left to the upper right region of Figure 6. Results are shown in Figure 10: for an immature pre-treatment phenotype in the current parameter regime, a perturbation to the VEGF production rate, α_v, has a superior anti-angiogenic effect compared to perturbations to the VEGF binding rate, k^v_{on}, or VEGF decay rate, δ_v. From this result we propose that decreasing the VEGF production rate by a factor of 50 is preferable to decreasing the VEGF binding rate by a factor of 100 or increasing the

VEGF clearance rate by a factor of 100 for effecting a transition from a highly angiogenic pre-treatment phenotype to a non-angiogenic phenotype.

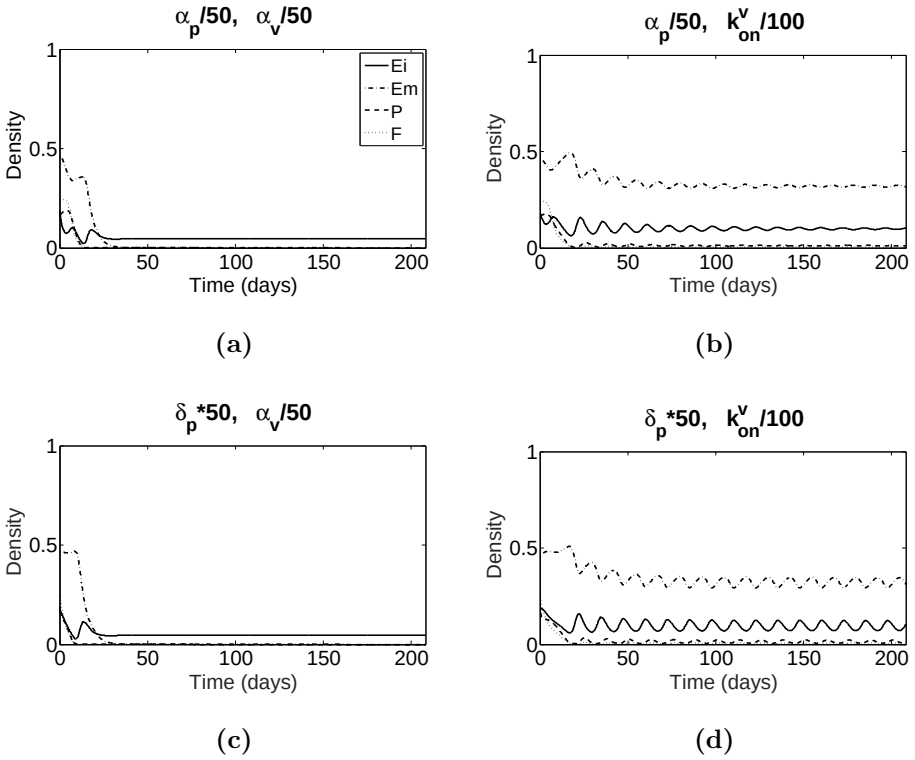

Figure 9: Simulations of theoretical anti-angiogenic treatments for vessels with the full model (equations (1)-(16)) starting in steady state (iv) show that perturbations to the VEGF production rate, α_v, and a perturbation to the PDGF production or clearance rates, α_p (a) or δ_p (c) respectively, lead to a transition from the angiogenic steady state (iv) towards steady state (i). Perturbations to the VEGF association rate, k^v_{on}, and α_p (b) or δ_p (d) lead to a transition from (iv) to (iii). The results for simulations where the VEGF clearance rate, δ_v, was multiplied by 100 were similar to the results for $k^v_{\text{on}}/100$, and are not shown here. The results for simulations where the PDGF clearance rate, k^p_{on}, was reduced by a factor of 50 were similar to the results for $\delta_p * 50$ and are not shown here. Initial conditions are the steady state values for all variables in (iv), all unperturbed parameters are taken from Table C1 and treatment begins at t=0.

In preclinical experiments, antibodies for VEGF and PDGF are administered at a dose such that a large percentage of the free ligand is neutralised, and tumour growth is inhibited by around 90% (Ferrara et al., 2005). The magnitude of the perturbations to the clearance rates of VEGF and PDGF in Figures 9 and 10 are such that the free VEGF or PDGF concentrations decrease to less than 30% of their pre-treatment concentrations, and that the fractional occupancy of VEGF receptors falls below the threshold for EC proliferation. Similarly, inhibitors of downstream effects of ligand binding, such as Sunitinib (see Section 1), significantly reduce the fractional occupancy of receptors (Speed

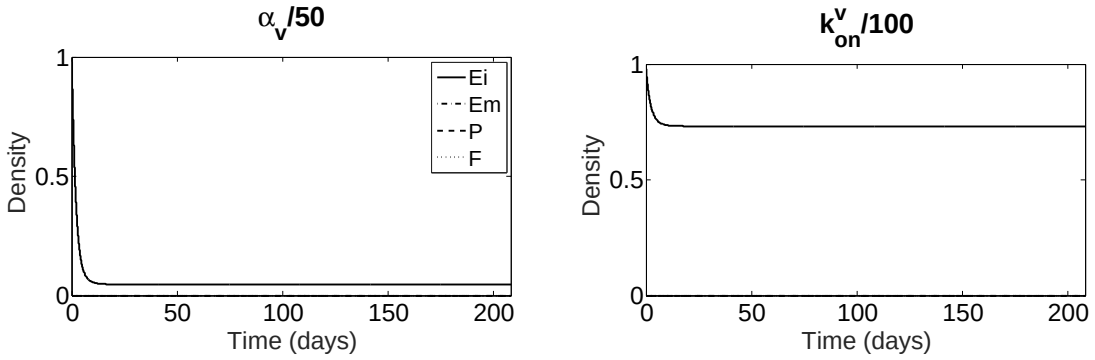

(a) **(b)**

Figure 10: Simulations of theoretical anti-angiogenic treatments using the full model (equations (1)-(16)) for the highly angiogenic pre-treatment phenotype (iii) show that a perturbation to the VEGF production rate, α_v, leads to a transition towards steady state (i), but a perturbation to the VEGF association rate, k^v_{on}, does not lead to a transition to a non-angiogenic steady state. The results for simulations where the VEGF clearance rate, δ_v, was multiplied by 100 were similar to $k^v_{\text{on}}/100$ and are not shown here. Initial conditions are the steady state values in (iii) for all variables, all unperturbed parameters are taken from Table C1, except $\kappa = 0.008h^{-1}$, and treatment begins at t=0.

et al., 2012). The magnitudes of the perturbations to binding rates of VEGF and PDGF are such that the post-treatment fractional occupancy of receptors is around 19%, which is below the threshold for proliferation in our model. Production rates of ligands are more difficult to measure in pre-clinical models, and the orders of magnitudes for our perturbations to the production rates of VEGF and PDGF by tumour cells and ECs respectively are order of magnitude estimates.

5 Discussion

Experimental and clinical results have shown that anti-angiogenic therapies as monotherapies are of limited value, while searches for biomarkers of angiogenic response to treatment in recent years have been unfruitful.

We have developed a complex ODE model representing the interactions between processes involved in angiogenesis, and the impact of the interactions on the effects of anti-angiogenic therapies on neovasculature. We have validated the full model qualitatively using experimental data but quantitative validation cannot yet be achieved due to high parameter dimensionality and poor data availability. A simplified version of the model was used to identify the expected long-term behaviour of the full model.

The steady state behaviours exhibited by the full and simplified models are physically realistic, representing vessel phenotypes (for high quality 3D images of tumour vessels that exhibit immature and normalised phenotypes, see Dobosz et al. (2014), and for our interpretation of phenotypical features, see Figure 1). We acknowledge that the full model may exhibit other steady state solutions in addition to the four solutions considered above. However, the high dimensional nature of the parameter space makes an analytical treatment of the full model impractical.

Simulation of anti-angiogenic treatment with the full model includes mechanistic detail, which is not possible to capture with the simplified model. Transitions from angiogenic phenotypes to non-angiogenic phenotypes are considered in this paper as an indication for response to treatment. If measurable, the pre-treatment and post-treatment phenotypes of vascular sub-regions could be used as a biomarker of response to treatment for preclinical experiments.

The conclusions that we draw from our investigations of our full and simplified models can be summarised as follows:

1. According to the simplified model, there are four possible long term behaviours for ECs and PCs in the parameter regimes studied. Two behaviours are angiogenic and two are non-angiogenic. The regions in which these solutions exist and are locally stable can be categorised according to the ratio of $\frac{\text{death rate}}{\text{growth rate}}$ for ECs and the same ratio for PCs. Similar long-term behaviour regimes exist for the full model and a direct comparison of the long term behaviour regimes of the simplified and full models illustrates this (see Figures 5 and 6).

2. The full model can reproduce qualitative experimental results of VEGF, Ang2 and combined VEGF/Ang2 inhibition with respect to the increase in PC coverage.

3. Of the perturbations we simulated, the most effective for moving from a normalised angiogenic steady state (iv) towards a non-angiogenic steady state (i) was to decrease the VEGF production rate and to decrease the rate of PDGF production or binding, or to increase the rate of PDGF clearance (see Figure 9).

4. Of the perturbations we simulated, the most effective for effecting a transition from a runaway angiogenic steady state similar to (iii) to a less angiogenic steady state (i), was to decrease the VEGF production rate (see Figure 10).

5. According to our model in the current parameter regime, combination anti-VEGF/anti-

Ang2 therapy has a synergistic effect when administered to a highly angiogenic pre-treatment phenotype, but not when administered to a normalised pre-treatment phenotype.

Our model was inspired by another model proposed by Zheng et al. (2013), which accounts for similar biochemical variables (VEGF, Ang1, Ang2, PDGF) while placing more focus on the biomechanical aspects of one-dimensional vessel growth, comparing model outputs with a corneal angiogenesis model. On the rationale that simplifying some aspects of the biology would yield a model that is analytically tractable, and with a lack of detailed spatially resolved data with which to validate our model, we chose a well-mixed approach. This approach led to a significant reduction in the total number of parameters in our model compared to Zheng et al. at the expense of spatial information. We adapted several features for our model, such as Ang2 dependent EC proliferation, the generation of receptors as cells proliferate, and loss as they die and the details of the exocytosis of Ang2 from WPBs. We also developed a new cell dynamics sub-model.

The identification of expected vascular phenotypes using mathematical analysis has formed the basis of our conclusions. We anticipate robustness of our results as it is the end states rather than the transients that are most important for our conclusions, and these end states are well understood from the simplified model analysis. Several mathematical models of angiogenesis recommend treatment on a one-size-fits-all basis, where treatment is applied to only one pre-treatment phenotype (Zheng et al., 2013, Billy et al., 2009, Jain et al., 2009). To the best of our knowledge, ours is the first mechanistic mathematical model of angiogenesis which considers the impact of anti-angiogenic treatment on different vascular phenotypes.

Aspects of angiogenesis that feature in other models include the role of immune cells such as macrophages (Levine et al., 2000), oxygen tension within the tumour (Lignet et al., 2013, Owen et al., 2009), blood flow (Stéphanou et al., 2005, Welter and Rieger, 2010, Perfahl et al., 2011) and the cell cycle (Perfahl et al., 2011). Importantly for the future of our work, the relationship between blood flow, oxygen tension and drug delivery has also been studied in theoretical models of angiogenesis (Welter and Rieger, 2013, Byrne et al., 2011). Furthermore, the important process of vessel regression following the detachment of pericytes is taken into account in several recent models (Welter and Rieger, 2010, 2013, Owen et al., 2009). We have chosen to include processes relevant to our aim of investigating the mechanistic basis of neovascularisation and normalisation via

a tractable ODE model, but incorporation of further aspects of angiogenic tumour growth, including those listed, will form the basis of future development of the full model. We note that taking into account spatial, temporal and network aspects of vascular tumour growth could yeild new insight into expected therapeutic outcomes for given pre-treatment phenotypes.

A limitation of the simplified and full models is that the detail of a heterogeneous tumour is not captured, since both models represent a small, well-mixed volume of tumour tissue. The phenotypes described in this paper apply to an individual, approximately homogeneous portion of the tumour. This limitation could explain the appearance of the extreme phenotypes, where one EC type predominates, exhibited by the full model. In reality, a tumour contains sections with different characteristics, and these regions are physically connected. The delivery of cytotoxic drugs to the tumour depends heavily on the topology of the vasculature. Incorporation of spatial features into our model could yield more insight into the expected outcome for different therapies and different pre-treatment phenotypes. For a review of spatial models of angiogenesis, see Scianna et al. (2013), Rieger et al. (2016). Models that focus on vessel architecture and the resultant drug delivery could be a useful starting point for a future hybrid model of vascular tumour growth.

In addition to the non-spatial nature of the model, we are limited by a shortage of suitable experimental data with which to estimate system parameters and validate our model. Accurate parameterisation and model validation are often challenges that face modellers of biological systems. Many of the parameters of the full model are estimated based on the resultant model behaviour, or taken from *in-vitro* studies. A 39-dimensional parameter space cannot be explored fully via current techniques, and therefore it is not feasible to conduct a global sensitivity analysis for the full model. We have attempted to remedy this via the analytical treatment of a simplified model, which yields information about the long term behaviours of the simplified and full models, and identifies parameters which have a significant impact on the model behaviour.

The phenotype-specific outcomes of our model simulations may be of direct clinical importance, and could prompt further experimental studies that would help to parameterise the full model. For example, proliferation and death rates of ECs and PCs were not available for *in-vivo* studies, but were shown to be critical to the model behaviour. Experiments that allow these rates to be measured would be valuable for the verification

of model outcomes.

The same experimental study that we used to validate our model showed that Crossmab treatment or anti-VEGF treatment led to a significant decrease in primary tumour volume, but anti-Ang2 treatment did not. Additionally, experimental results showed that, for progressed tumours, the metastatic load in the liver was significantly reduced by both anti-Ang2 and combination therapies. The inclusion of tumour cells in the model could enhance the understanding of the role played by angiogenesis in the growth and spread of cancer cells. Since tumour size is measured in most preclinical experiments relating to anti-angiogenic therapies, we may hope for further validation of the model with the inclusion of a tumour compartment. Inspiration may be drawn from several recent models of angiogenesis that also account for tumour growth (Billy et al., 2009, Ribba et al., 2011, Lignet et al., 2013, Perfahl et al., 2011, Jain et al., 2009, Welter et al., 2009, Bartha and Rieger, 2006).

In its current form, our model represents, and has been qualitatively validated against, pre-clinical experimental systems, although most parameters were obtained from *in-vitro* studies. However, since we opted for a non-spatial approach, it could be used as a generic model to describe key processes of neovascularisation of tumours in, for example, clinical studies, or it could be adapted to represent other situations where angiogenesis occurs, such as in diabetic retinopathy, wound healing or developmental biology.

There has been extensive work in recent years to identify biomarkers of response to anti-angiogenic therapies, with little success (Murukesh et al., 2010). As experimental technology advances, the possibility to measure a pre-treatment vascular phenotype of tumour sub-regions becomes more realistic. From the results of our simulations and model analysis, we hypothesize that different pre-treatment vascular phenotypes will respond differently to different anti-angiogenic therapies. The predominant vascular structure within a tumour could be used as a biomarker of angiogenic response to treatment, since a switch in phenotype is a goal of the therapies simulated in this paper.

We have demonstrated that a well-mixed model can generate valuable and meaningful results in the absence of spatial information. Taking into account the morphological phenotype of tumour regions, we are able to make predictions regarding appropriate "personalised" anti-angiogenic treatments. As technology advances, the measurement of *in-vivo* tumour vessel densities using techniques such as ultramicroscopy (Dobosz et al., 2014) could be used to the validate and parameterise our model, and thereby accelerate

906 the development of anti-angiogenic therapies for pre-clinical models.

907 Acknowledgements

908 The authors wish to acknowledge Benjamin Ribba for useful discussions. L.G.H ac-
909 knowledges the financial support of the University of Oxford, the Systems Approaches
910 to Biomedical Sciences Centre for Doctoral Training (SABS-CDT), the UK Engineering
911 and Physical Sciences Research Council (EPSRC grant number EP/G037280/1) and F.
912 Hoffman La-Roche Ltd.

913 Author's contributions

914 L.G.H., E.A.G., H.M.B., P.K.M., A. P. and J.W. conceived of and contributed to the de-
915 velopment of the mathematical model. L.G.H. implemented and parametrized the math-
916 ematical model, carried out simulations and wrote the first draft of the manuscript. All
917 authors agree with manuscript results and conclusions. All authors made critical revisions
918 and approved the final version.

References

Agur, Z., Arakelyan, L., Daugulis, P., and Ginosar, Y. (2003). Hopf point analysis for angiogenesis models. *Discrete and Continuous Dynamical Systems - Series B*, 4(1):29–38.

Armulik, A., Abramsson, A., and Betsholtz, C. (2005). Endothelial/pericyte interactions. *Circulation Research*, 97(6):512–23.

Audero, E., Cascone, I., Zanon, I., Previtali, S. C., Piva, R., Schiffer, D., and Bussolino, F. (2001). Expression of Angiopoietin-1 in human glioblastomas regulates tumor-induced angiogenesis: in vivo and in vitro studies. *Arteriosclerosis, Thrombosis, and Vascular Biology*, 21(4):536–541.

Bartha, K. and Rieger, H. (2006). Vascular network remodeling via vessel cooption, regression and growth in tumors. *Journal of theoretical biology*, 241(4):903–18.

Billy, F., Ribba, B., Saut, O., Morre-Trouilhet, H., Colin, T., Bresch, D., Boissel, J.-P., Grenier, E., and Flandrois, J.-P. (2009). A pharmacologically based multiscale mathematical model of angiogenesis and its use in investigating the efficacy of a new cancer treatment strategy. *Journal of Theoretical Biology*, 260(4):545–562.

Bogdanovic, E., Nguyen, V. P. K. H., and Dumont, D. J. (2006). Activation of Tie2 by angiopoietin-1 and angiopoietin-2 results in their release and receptor internalization. *Journal of Cell Science*, 119(17):3551–3560.

Byrne, H. M., Owen, M. R., Alarcon, T., Murphy, J., and Maini, P. K. (2011). MODELLING THE RESPONSE OF VASCULAR TUMOURS TO CHEMOTHERAPY: A MULTISCALE APPROACH. *Mathematical Models and Methods in Applied Sciences*.

Cook, K. M. and Figg, W. D. (2010). Angiogenesis inhibitors: current strategies and future prospects. *CA: A Cancer Journal for Clinicians*, 60(4):222–43.

Cunningham, S. A. (1999). Characterization of Vascular Endothelial cell Growth Factor interactions with the kinase insert domain-containing receptor tyrosine kinase. A real time kinetic study. *Journal of Biological Chemistry*, 274(26):18421–18427.

Dickson, P. V., Hamner, J. B., Sims, T. L., Fraga, C. H., Ng, C. Y. C., Rajasekeran, S., Hagedorn, N. L., McCarville, M. B., Stewart, C. F., and Davidoff, A. M. (2007). Bevacizumab-induced transient remodeling of the vasculature in neuroblastoma xenografts results in improved delivery and efficacy of systemically administered C chemotherapy. *Clinical Cancer Research*, 13(13):3942–3950.

Dobosz, M., Ntziachristos, V., Scheuer, W., and Strobel, S. (2014). Multispectral fluorescence ultramicroscopy : three- dimensional visualization and automatic quantification of tumor morphology , drug penetration , and antiangiogenic treatment response. *Neoplasia*, 16(1):1–13, IN1–IN7.

Du Bois, A., Floquet, A., Kim, J. W., Rau, J., Del Campo, J. M., Friedlander, M., Pignata, S., Fujiwara, K., Vergote, I., Colombo, N., Mirza, M. R., Monk, B. J., Wimberger, P., Ray-Coquard, I., Zang, R., Diaz-Padilla, I., Baumann, K. H., Kim, J. H., and Harter, P. (2013). Randomized, double-blind, phase III trial of pazopanib versus placebo in women who have not progressed after first-line chemotherapy for advanced epithelial ovarian, fallopian tube, or primary peritoneal cancer (AEOC): Results of an international Intergro. In *Proceedings of American Society of Clinical Oncology*.

Falcón, B. L., Hashizume, H., Koumoutsakos, P., Chou, J., Bready, J. V., Coxon, A., Oliner, J. D., McDonald, D. M., Falcon, B. L., Hashizume, H., Koumoutsakos, P., Chou, J., Brady, J. V., Coxon, A., Oliner, J. D., and McDonald, D. M. (2009). Contrasting actions of selective inhibitors of angiopoietin-1 and angiopoietin-2 on the normalization of tumor blood vessels. *The American Journal of Pathology*, 175(5):2159–70.

Ferrara, N., Gerber, H.-P., and LeCouter, J. (2003). The biology of VEGF and its receptors. *Nature Medicine*, 9(6):669–76.

Ferrara, N., Hillan, K. J., and Novotny, W. (2005). Bevacizumab (Avastin), a humanized anti-VEGF monoclonal antibody for cancer therapy. *Biochemical and Biophysical Research Communications*, 333(2):328–35.

Fiedler, U., Scharpfenecker, M., Koidl, S., Hegen, A., Grunow, V., Schmidt, J. M., Kriz, W., Thurston, G., and Augustin, H. G. (2004). The Tie-2 ligand angiopoietin-2 is stored in and rapidly released upon stimulation from endothelial cell Weibel-Palade bodies. *Blood*, 103(11):4150–6.

Folkman, J. (1971). Tumor angiogenesis: therapeutic implications. *The New England Journal of Medicine*, 285:1182–1186.

Fox, P. L. and DiCorletto, P. E. (1984). Regulation of production of a platelet-derived growth factor-like protein by cultured bovine aortic endothelial cells. *Journal of Cellular Physiology*, 308.

Fuxe, J., Tabruyn, S., Colton, K., Zaid, H., Adams, A., Baluk, P., Lashnits, E., Morisada, T., Le, T., O'Brien, S., Epstein, D. M., Koh, G. Y., and McDonald, D. M. (2011). Pericyte requirement for anti-leak action of angiopoietin-1 and vascular remodeling in sustained inflammation. *The American Journal of Pathology*, 178(6):2897–2909.

Goel, S., Duda, D., Xu, L., and Munn, L. (2011). Normalization of the vasculature for treatment of cancer and other diseases. *Physiol Rev*, 91(3):1071–1121.

Goodman, V. L., Rock, E. P., Dagher, R., Ramchandani, R. P., Abraham, S., Gobburu, J. V. S., Booth, B. P., Verbois, S. L., Morse, D. E., Liang, C. Y., Chidambaram, N., Jiang, J. X., Tang, S., Mahjoob, K., Justice, R., and Pazdur, R. (2007). Approval summary: sunitinib for the treatment of imatinib refractory or intolerant gastrointestinal stromal tumors and advanced renal cell carcinoma. *Clinical Cancer Research*, 13(5):1367–73.

Han, Y. S., Lee, J. E., Jung, J. W., and Lee, J. S. (2009). Inhibitory effects of bevacizumab on angiogenesis and corneal neovascularization. *Graefe's Archive for Clinical and Experimental Ophthalmology*, 247(4):541–8.

Holash, J., Maisonpierre, P. C., Compton, D., Boland, P., Alexander, C. R., Zagzag, D., Yancopoulos, G. D., and Wiegand, S. J. (1999). Vessel cooption, regression, and growth in tumors mediated by angiopoietins and VEGF. *Science*, 284(5422):1994–8.

Inai, T., Mancuso, M., Hashizume, H., Baffert, F., Haskell, A., Baluk, P., Hu-Lowe, D. D., Shalinsky, D. R., Thurston, G., Yancopoulos, G. D., and McDonald, D. M. (2004). Inhibition of Vascular Endothelial Growth Factor (VEGF) signaling in cancer causes loss of endothelial fenestrations, regression of tumor vessels, and appearance of basement membrane ghosts. *The American Journal of Pathology*, 165(1):35–52.

Jain, H., Nör, J., and Jackson, T. (2008). Modeling the VEGFBcl-2CXCL8 Pathway inIntratumoral Agiogenesis. *Bulletin of Mathematical Biology*, 70(1):89–117.

Jain, H. V., Nör, J. E., and Jackson, T. L. (2009). Quantification of endothelial cell-targeted anti Bcl-2 therapy and its suppression of tumor growth and vascularization. *Molecular Cancer Therapeutics*, 8(10):2926–2936.

Jain, R. K. (2001). Normalizing tumor vasculature with anti-angiogenic therapy: a new paradigm for combination therapy. *Nature Medicine*, 7(9):987–989.

Jain, R. K. (2005). Normalization of tumor vasculature: an emerging concept in antiangiogenic therapy. *Science*, 307(5706):58–62.

Kienast, Y., Klein, C., Scheuer, W., Raemsch, R., Lorenzon, E., Bernicke, D., Herting, F., Yu, S., The, H. H., Martarello, L., Gassner, C., Stubenrauch, K.-G. G., Munro, K., Augustin, H. G., and Thomas, M. (2013). Ang-2-VEGF-A CrossMab, a novel bispecific human IgG1 antibody blocking VEGF-A and Ang-2 functions simultaneously, mediates potent antitumor, antiangiogenic, and antimetastatic efficacy. *Clinical Cancer Research*, 19(24):6730–6740.

Levine, H. A., Sleeman, B. D., and Nilsen-Hamilton, M. (2000). A mathematical model for the roles of pericytes and macrophages in the initiation of angiogenesis. I. The role of protease inhibitors in preventing angiogenesis. *Mathematical Biosciences*, 168(1):77–115.

Lignet, F., Benzekry, S., Wilson, S., Billy, F., Saut, O., Tod, M., You, B., Adda Berkane, A., Kassour, S., Wei, M. X., Grenier, E., and Ribba, B. (2013). Theoretical investigation of the efficacy of antiangiogenic drugs combined to chemotherapy in xenografted mice. *Journal of Theoretical Biology*, 320:86–99.

Lobov, I. B., Brooks, P. C., and Lang, R. A. (2002). Angiopoietin-2 displays VEGF-dependent modulation of capillary structure and endothelial cell survival in vivo. *Proceedings of the National Academy of Sciences*, 99(17):11205–11210.

Mac Gabhann, F., Yang, M. T., and Popel, A. S. (2005). Monte Carlo simulations of VEGF binding to cell surface receptors in vitro. *Biochimica et Biophysica Acta*, 1746(2):95–107.

Maisonpierre, P. C. (1997). Angiopoietin-2, a natural antagonist for Tie2 that disrupts in vivo angiogenesis. *Science*, 277(5322):55–60.

Matsumoto, S., Saito, K., Takakusagi, Y., Matsuo, M., Munasinghe, J. P., Morris, H. D., Lizak, M. J., Merkle, H., Yasukawa, K., Devasahayam, N., Suburamanian, S., Mitchell, J. B., and Krishna, M. C. (2014). In vivo imaging of tumor physiological, metabolic, and redox changes in response to the anti-angiogenic agent sunitinib: longitudinal assessment to identify transient vascular renormalization. *Antioxidants & Redox Signaling*, 21(8):1145–1155.

Matsushita, K., Yamakuchi, M., Morrell, C. N., Ozaki, M., O'Rourke, B., Irani, K., and Lowenstein, C. J. (2005). Vascular endothelial growth factor regulation of Weibel-Palade-body exocytosis. *Blood*, 105(1):207–14.

Milde, F., Lauw, S., Koumoutsakos, P., and Iruela-Arispe, M. L. (2013). The mouse retina in 3D: quantification of vascular growth and remodeling. *Integrative biology*, 5(12):1426–38.

Monk, B. J., Poveda, A., Vergote, I., Raspagliesi, F., Fujiwara, K., Bae, D.-S., Oaknin, A., Ray-Coquard, I., Provencher, D. M., Karlan, B. Y., Lhommé, C., Richardson, G., Rincón, D. G., Coleman, R. L., Herzog, T. J., Marth, C., Brize, A., Fabbro, M., Redondo, A., Bamias, A., Tassoudji, M., Navale, L., Warner, D. J., and Oza, A. M. (2014). Anti-angiopoietin therapy with trebananib for recurrent ovarian cancer (TRINOVA-1): a randomised, multicentre, double-blind, placebo-controlled phase 3 trial. *The Lancet. Oncology*, 15(8):799–808.

Murukesh, N., Dive, C., and Jayson, G. C. (2010). Biomarkers of angiogenesis and their role in the development of VEGF inhibitors. *British Journal of Cancer*, 102(1):8–18.

NCI (2014). http://www.cancer.gov/cancertopics/druginfo/fda-bevacizumab.

Nishino, M., Giobbie-Hurder, A., Ramaiya, N. H., and Hodi, F. S. (2014). Response assessment in metastatic melanoma treated with ipilimumab and bevacizumab: CT tumor size and density as markers for response and outcome. *Journal for immunotherapy of cancer*, 2(1):40.

Owen, M., Alarcón, T., Maini, P., and Byrne, H. (2009). Angiogenesis and vascular remodelling in normal and cancerous tissues. *Journal of Mathematical Biology*, 58(4-5):689–721.

Park, S. W., Yun, J.-H., Kim, J. H., Kim, K.-W., Cho, C.-H., and Kim, J. H. (2014). Angiopoietin 2 induces pericyte apoptosis via $\alpha 3\beta 1$ integrin signaling in diabetic retinopathy. *Diabetes*, 63(9):3057–3068.

Perfahl, H., Byrne, H. M., Chen, T., Estrella, V., Alarcón, T., Lapin, A., Gatenby, R. a., Gillies, R. J., Lloyd, M. C., Maini, P. K., Reuss, M., and Owen, M. R. (2011). Multiscale modelling of vascular tumour growth in 3D: the roles of domain size and boundary conditions. *PloS One*, 6(4):e14790–e14790.

Plank, M. J., Sleeman, B. D., and Jones, P. F. (2004). A mathematical model of tumour angiogenesis, regulated by vascular endothelial growth factor and the angiopoietins. *Journal of Theoretical Biology*, 229(4):435–54.

Prokopiou, S. A. (2013). *Integrative modelling of angiogenesis in the bovine corpus luteum.* PhD thesis, University of Nottingham.

Raymond, E., Dahan, L., Raoul, J.-L., Bang, Y.-J., Borbath, I., Lombard-Bohas, C., Valle, J., Metrakos, P., Smith, D., Vinik, A., Chen, J.-S., Hörsch, D., Hammel, P., Wiedenmann, B., Van Cutsem, E., Patyna, S., Lu, D. R., Blanckmeister, C., Chao, R., and Ruszniewski, P. (2011). Sunitinib Malate for the treatment of pancreatic neuroendocrine tumors. *New England Journal of Medicine*, 364(6):501–513.

Ribba, B., Watkin, E., Tod, M., Girard, P., Grenier, E., You, B., Giraudo, E., and Freyer, G. (2011). A model of vascular tumour growth in mice combining longitudinal tumour size data with histological biomarkers. *European Journal of Cancer*, 47(3):479–90.

Rieger, H., Fredrich, T., and Welter, M. (2016). Physics of the tumor vasculature: Theory and experiment. *The European Physical Journal Plus*, 131(2):31.

Rivera, L. B. and Bergers, G. (2015). CANCER. Tumor angiogenesis, from foe to friend. *Science*, 349(6249):694–5.

Scharpfenecker, M., Fiedler, U., Reiss, Y., and Augustin, H. G. (2005). The Tie-2 ligand angiopoietin-2 destabilizes quiescent endothelium through an internal autocrine loop mechanism. *Journal of cell science*, 118(Pt 4):771–80.

Scianna, M., Bell, C. G., and Preziosi, L. (2013). A review of mathematical models for the formation of vascular networks. *Journal of Theoretical Biology*, 333:174–209.

Serini, G., Ambrosi, D., Giraudo, E., Gamba, A., Preziosi, L., and Bussolino, F. (2003). Modeling the early stages of vascular network assembly. *The EMBO Journal*, 22(8):1771–1779.

Speed, B., Bu, H.-Z., Pool, W. F., Peng, G. W., Wu, E. Y., Patyna, S., Bello, C., and Kang, P. (2012). Pharmacokinetics, distribution, and metabolism of [14C]sunitinib in rats, monkeys, and humans. *Drug metabolism and disposition: the biological fate of chemicals*, 40(3):539–55.

Stéphanou, a., McDougall, S., a.R.a. Anderson, and Chaplain, M. (2005). Mathematical modelling of flow in 2D and 3D vascular networks: Applications to anti-angiogenic and chemotherapeutic drug strategies. *Mathematical and Computer Modelling*, 41(10):1137–1156.

Thomas, M., Kienast, Y., Scheuer, W., Bähner, M., Kaluza, K., Gassner, C., Herting, F., Brinkmann, U., Seeber, S., Kavlie, A., Welschof, M., Ries, S., Weidner, K. M., Regula, J. T., and Klein, C. (2013). A novel angiopoietin-2 selective fully human antibody with potent anti-tumoral and anti-angiogenic efficacy and superior side effect profile compared to Pan-Angiopoietin-1/-2 inhibitors. *PloS One*, 8(2):e54923.

Wakui, S., Yokoo, K., Muto, T., Suzuki, Y., Takahashi, H., Furusato, M., Hano, H., Endou, H., and Kanai, Y. (2006). Localization of Ang-1, -2, Tie-2, and VEGF expression at endothelial-pericyte interdigitation in rat angiogenesis. *Laboratory Investigation; a Journal of Technical Methods and Pathology*, 86(11):1172–84.

Wang, D., Lehman, R. E., Donner, D. B., Matli, M. R., Warren, R. S., and Welton, M. L. (2002). Expression and endocytosis of VEGF and its receptors in human colonic vascular endothelial cells. *American Journal of Physiology - Gastrointestinal and Liver Physiology*, 282(6):G1088–G1096.

Weiss, K. D. (2004). US Food and Drug Administration, Centre for drug evaluation and research. STN-125085-0.

Welter, M., Bartha, K., and Rieger, H. (2009). Vascular remodelling of an arterio-venous blood vessel network during solid tumour growth. *Journal of theoretical biology*, 259(3):405–22.

Welter, M. and Rieger, H. (2010). Physical determinants of vascular network remodeling during tumor growth. *The European physical journal. E, Soft matter*, 33(2):149–63.

Welter, M. and Rieger, H. (2013). Interstitial fluid flow and drug delivery in vascularized tumors: a computational model. *PloS one*, 8(8):e70395.

Wong, P.-P., Demircioglu, F., Ghazaly, E., Alrawashdeh, W., Stratford, M. R. L., Scudamore, C. L., Cereser, B., Crnogorac-Jurcevic, T., McDonald, S., Elia, G., Hagemann, T., Kocher, H. M., and Hodivala-Dilke, K. M. (2015). Dual-action combination therapy enhances angiogenesis while reducing tumor growth and spread. *Cancer cell*, 27(1):123–37.

Zheng, X., Young Koh, G., and Jackson, T. (2013). A continuous model of angiogenesis: Initiation, extension, and maturation of new blood vessels modulated by vascular endothelial growth factor, angiopoietins, platelet-derived growth factor-B, and pericytes. *Discrete and Continuous Dynamical Systems - Series B*, 18(4):1109–1154.

A Biological feasibility of steady states (iv) and (v)

In Section 3.1, we identified two steady state solutions to equations (17)-(20) where all cell types coexist. Here, we aim to identify regions of parameter space in which steady states (iv) and (v) are physically realistic.

The solutions $P_\pm$ are the roots of equation (21) and can be written

$$P_\pm = \frac{1}{2}\left[-a \pm \sqrt{a^2 - 4b}\right]$$

where

$$a = \left[\left(E_0\left(1 - \frac{\hat{\rho}}{\hat{\theta}}\right) - P_0\left(1 - \frac{\hat{\epsilon}}{\hat{\kappa}}\right)\right) + \frac{(\nu + \hat{\epsilon})}{\zeta}\right]$$

and

$$b = P_0\left[\frac{\hat{\epsilon}}{\hat{\kappa}}E_0\left(1 - \frac{\hat{\rho}}{\hat{\theta}}\right) - \left(1 - \frac{\hat{\epsilon}}{\hat{\kappa}}\right)\frac{(\nu + \hat{\epsilon})}{\zeta}\right].$$

For physically realistic solutions, we require that $P_\pm \in \mathbb{R}_0^+$. Using the corresponding solutions for E_i, E_m, E_P given in section 3.1, for $E_P > 0$, we require $\frac{\hat{\rho}}{\hat{\theta}} < 1$ for biological feasibility. The solutions for $P_\pm$ can be classified as follows:

Case 1 $a^2 > 4b \quad \rightarrow \quad P_\pm \in \mathbb{R}$:

- **Case 1.1** $b > 0$:
  - **Case 1.1.1** $a < 0 \quad \rightarrow \quad P_+ > P_- > 0$: two positive roots;
  - **Case 1.1.2** $a > 0 \quad \rightarrow \quad P_\pm < 0$: two negative roots;
- **Case 1.2** $b < 0$:
  - **Case 1.2.1** $a < 0 \quad \rightarrow \quad P_+ > 0; P_- < 0$: one positive, one negative root.
  - **Case 1.2.2** $a > 0 \quad \rightarrow \quad P_+ > 0; P_- < 0$: one positive, one negative root;
  - **Case 1.2.3** $a = 0 \quad \rightarrow \quad P_+ > 0; P_- < 0$: one positive, one negative root;

Case 2 $a^2 - 4b < 0 \quad \rightarrow \quad P_+, P_- \in \mathbb{C}$: no real roots;

Having established where physically realistic steady state solutions for $P_\pm$ exist, we now proceed to establish, for each case, whether the corresponding values for the other dependent variables are also physically realistic. For **Case 1.1.1**, where both $P_\pm \in \mathbb{R}_0^+$, the model parameters must satisfy

$$\frac{\hat{\kappa}}{\hat{\epsilon}}\left(\frac{\nu+\hat{\epsilon}}{\zeta}\right)\left(1-\frac{\hat{\epsilon}}{\hat{\kappa}}\right) < E_0\left(1-\frac{\hat{\rho}}{\hat{\theta}}\right) < P_0\left(1-\frac{\hat{\epsilon}}{\hat{\kappa}}\right) - \left(\frac{\nu+\hat{\epsilon}}{\zeta}\right), \tag{A.1}$$

or, equivalently,

$$\frac{\nu+\hat{\epsilon}}{\zeta} < P_0\frac{\hat{\epsilon}}{\hat{\kappa}}\left(1-\frac{\hat{\epsilon}}{\hat{\kappa}}\right).$$

We conclude that a necessary condition for feasible solutions for **Case 1.1.1** is that $\frac{\hat{\epsilon}}{\hat{\kappa}} < 1$. Fixing values for ζ, E_0, P_0 and ν from current parameter set, defined in Table 2, condition (A.1) is never satisfied where $\frac{\hat{\rho}}{\hat{\theta}} < 1$ and $\frac{\hat{\epsilon}}{\hat{\kappa}} < 1$. Therefore the conditions for **Case 1.1.1** are not met and we do not expect real, positive solutions for steady solution (v) using the current parameter set.

In **Case 1.2.1**, **Case 1.2.2** and **Case 1.2.3**, where $b < 0$, the condition

$$\left(\frac{\hat{\kappa}}{\hat{\epsilon}} - 1\right)(\nu+\hat{\epsilon}) > \zeta E_0\left(1-\frac{\hat{\rho}}{\hat{\theta}}\right) \tag{A.2}$$

must hold for a biologically realistic solution for (iv). In the feasible region, $a^2 - 4b > 0$ is always satisfied since $b < 0$. From inequality (A.2) and the requirement that $\frac{\hat{\rho}}{\hat{\theta}} < 1$ for $E_P > 0$ in solution (iv), it follows that $\frac{\hat{\epsilon}}{\hat{\kappa}} < 1$ is a necessary condition for a feasible solution to (iv). For a positive, real solution for P_+, the feasible region of parameter space is defined by the intersection of $\frac{\hat{\rho}}{\hat{\theta}} < 1$, $\frac{\hat{\epsilon}}{\hat{\kappa}} < 1$ and the inequality (A.2).

B Linear stability analysis

Since there are multiple steady states that are biologically realistic in some regions of parameter space, we wish to perform a linear stability analysis in order to assess whether bistability may occur for some parameter values.

Figure 4 summarises the regions of parameter space according to ratios of $\frac{\hat{\rho}}{\hat{\theta}}$ and $\frac{\hat{\epsilon}}{\hat{\kappa}}$ where each of solutions (i)-(iv) is biologically feasible and/or linearly stable for the parameter values listed in Table 2, and the regions are labelled *A*-*D*.

The local stability of the steady states is determined by linearising the system of equations (17)-(20) to perturbations to the steady states by a small parameter, $0 < \omega \ll 1$, and seeking solutions of the form

$$(E_i, E_m, E_P, P) = (E_i^*, E_m^*, E_P^*, P^*) + \omega(\tilde{E}_i, \tilde{E}_m, \tilde{E}_P, \tilde{P})e^{\psi t},$$

where $(E_i^*, E_m^*, E_P^*, P^*)$ are the steady state concentrations and $(\tilde{E}_i, \tilde{E}_m, \tilde{E}_P, \tilde{P})$ represent correction terms. The sign of the real part of ψ determines whether correction terms grow or decay, and thus whether the steady state is locally stable. The values for ψ are the eigenvalues of the associated Jacobian matrix of the linearised system, J, where

$$J = \begin{pmatrix} \tilde{\theta} - \hat{\rho} + \zeta P - \hat{\eta} & -\hat{\theta}\frac{E_i}{E_0} + \hat{\mu} & -\zeta E_i & -\hat{\theta}\frac{E_i}{E_0} + \nu + \hat{\epsilon} \\ \hat{\eta} & \zeta P - \hat{\mu} & -\zeta E_m & 0 \\ -\zeta P & -\zeta P & \tilde{\kappa} - \hat{\epsilon} - \zeta(E_i + E_m) & -\hat{\kappa}\frac{P}{P_0} + \nu \\ \zeta P & \zeta P & \zeta(E_i + E_m) & -(\nu + \hat{\epsilon}) \end{pmatrix},$$

and where $\tilde{\theta} = \hat{\theta}\left(1 - \frac{(2E_i + E_m + E_P)}{E_0}\right)$, $\tilde{\kappa} = \hat{\kappa}\left(1 - \frac{(E_P + 2P)}{P_0}\right)$. If $\Re(\psi_j) < 0 \quad \forall j$, then the steady state solution is linearly stable. If any $\Re(\psi_j) \geq 0$ then the steady state solution is linearly unstable to leading order in ω.

We first analyse the linear stability of solutions (i)-(iii) (defined in Section 3.1), when one or more cell type is zero, then we analyse solution (iv), where all cell types coexist. The parameter combinations $\frac{\hat{\rho}}{\hat{\theta}}$ and $\frac{\hat{\epsilon}}{\hat{\kappa}}$ are used as bifurcation parameters and we examine the stability of the steady states, for the regions where they are biologically feasible, in parameter regimes defined by these ratios.

From the eigenvalues of the Jacobian evaluated at the trivial steady state, (i), the steady state is stable for $\frac{\hat{\rho}}{\hat{\theta}} > 1, \frac{\hat{\epsilon}}{\hat{\kappa}} > 1$, but unstable in all other parameter regions to leading order in ω. The eigenvalues, ψ, of the Jacobian evaluated at (i) are

$\psi_{i1} = -(\nu + \hat{\epsilon})$; $\qquad \psi_{i2} = \hat{\kappa} - \hat{\epsilon}$;

$$\psi_{i3} = \frac{1}{2}\left[(\hat{\theta} - \hat{\rho} - \hat{\eta} - \hat{\mu}) + \sqrt{(\hat{\theta} - \hat{\rho} - \hat{\eta} - \hat{\mu})^2 + 4\hat{\mu}(\hat{\theta} - \hat{\rho})}\right];$$

$$\psi_{i4} = \frac{1}{2}\left[(\hat{\theta} - \hat{\rho} - \hat{\eta} - \hat{\mu}) - \sqrt{(\hat{\theta} - \hat{\rho} - \hat{\eta} - \hat{\mu})^2 + 4\hat{\mu}(\hat{\theta} - \hat{\rho})}\right].$$

The linear stability of (i) depends on the ratios $\frac{\hat{\rho}}{\hat{\theta}}$ and $\frac{\hat{\epsilon}}{\hat{\kappa}}$. If $(\hat{\theta} - \hat{\rho} - \hat{\eta} - \hat{\mu})^2 + 4\hat{\mu}(\hat{\theta} - \hat{\rho}) > 0$,

- $\frac{\hat{\rho}}{\hat{\theta}} < 1, \quad \frac{\hat{\epsilon}}{\hat{\kappa}} < 1$: not linearly stable;
- $\frac{\hat{\rho}}{\hat{\theta}} < 1, \quad \frac{\hat{\epsilon}}{\hat{\kappa}} > 1$: not linearly stable;
- $\frac{\hat{\rho}}{\hat{\theta}} > 1, \quad \frac{\hat{\epsilon}}{\hat{\kappa}} < 1$: not linearly stable;
- $\frac{\hat{\rho}}{\hat{\theta}} > 1, \quad \frac{\hat{\epsilon}}{\hat{\kappa}} > 1$: linearly stable fixed point,

or alternatively if $(\hat{\theta} - \hat{\rho} - \hat{\eta} - \hat{\mu})^2 + 4\hat{\mu}(\hat{\theta} - \hat{\rho}) < 0$, it follows that $\frac{\hat{\rho}}{\hat{\theta}} > 1$, and the equilibrium

takes the form

- $\frac{\hat{\rho}}{\hat{\theta}} > 1, \quad \frac{\hat{\epsilon}}{\hat{\kappa}} < 1$: unstable spiral;
- $\frac{\hat{\rho}}{\hat{\theta}} > 1, \quad \frac{\hat{\epsilon}}{\hat{\kappa}} > 1$: stable spiral.

It is biologically realistic that when the death rates of ECs and PCs are both greater than their respective proliferation rates, there is a stable steady state where $E_i = E_m = P = E_P = 0$. In the other regimes, where the proliferation rates of ECs and/or PCs are greater than the corresponding death rates, the trivial steady state is unstable to perturbations along the eigenvectors of the Jacobian matrix with corresponding eigenvalues where $\Re(\psi) \geq 0$.

For the remaining steady states, the values of parameters are fixed to those in Table 2. As explained in Appendix A, solution (v) does not occur for the parameter values in Table 2. For steady states (ii) and (iv), the eigenvalues are calculated numerically in Matlab, and for (iii), they are calculated analytically. The steady state solution (ii), where all cell types except free PCs are absent, is linearly stable in region D (defined in Figure 4), where $\frac{\hat{\rho}}{\hat{\theta}} > 1$ and $\frac{\hat{\epsilon}}{\hat{\kappa}} < 1$ in the current parameter regime. Biologically, this is a non-angiogenic phenotype and it suggests in the absence of ECs, free PCs remain in the tumour region and may continue to proliferate. Although we do not include spatial effects in the current model, we propose that PCs may migrate to neighbouring tumour regions where $E_i, E_m \neq 0$ to normalise the vasculature.

The eigenvalues of the Jacobian matrix evaluated at (iii) can be found by obtaining the eigenvalues of the sub-matrices of the Jacobian, evaluated at (iii), which are

$$J_{iiia} = \begin{pmatrix} \hat{\theta}\left(1 - \frac{(2E_i + E_m)}{E_0}\right) - \hat{\rho} - \hat{\eta} & -\hat{\theta}\frac{E_i}{E_0} + \hat{\mu} \\ \hat{\eta} & -\hat{\mu} \end{pmatrix},$$

and

$$J_{iiib} = \begin{pmatrix} \hat{\kappa} - \hat{\epsilon} - \zeta(E_i + E_m) & +\nu \\ \zeta(E_i + E_m) & -(\nu + \hat{\epsilon}) \end{pmatrix}.$$

The eigenvalues of the Jacobian evaluated at (iii) are, therefore

$$\psi_{iii1}=-(\eta+\hat{\mu}),$$

$$\psi_{iii2}=\frac{\hat{\mu}(\hat{\rho}-\hat{\theta})}{\hat{\eta}+\hat{\mu}},$$

$$\psi_{iii3}=-\frac{1}{2}\left(\nu+2\hat{\epsilon}-\hat{\kappa}+\zeta E_0\left(1-\frac{\hat{\rho}}{\hat{\theta}}\right)\right)$$
$$+\frac{1}{2}\sqrt{\left(\nu+2\hat{\epsilon}-\hat{\kappa}+\zeta E_0\left(1-\frac{\hat{\rho}}{\hat{\theta}}\right)\right)^2-4(\nu+\hat{\epsilon})(\hat{\epsilon}-\hat{\kappa})+\hat{\epsilon}\zeta E_0\left(1-\frac{\hat{\rho}}{\hat{\theta}}\right)},$$

$$\psi_{iii4}=-\frac{1}{2}\left(\nu+2\hat{\epsilon}-\hat{\kappa}+\zeta E_0\left(1-\frac{\hat{\rho}}{\hat{\theta}}\right)\right)$$
$$-\frac{1}{2}\sqrt{\left(\nu+2\hat{\epsilon}-\hat{\kappa}+\zeta E_0\left(1-\frac{\hat{\rho}}{\hat{\theta}}\right)\right)^2-4(\nu+\hat{\epsilon})(\hat{\epsilon}-\hat{\kappa})+\hat{\epsilon}\zeta E_0\left(1-\frac{\hat{\rho}}{\hat{\theta}}\right)}.$$

From ψ_{iii3} and ψ_{iii4} we identify a region of linear stability of (iii) bounded by $\frac{\hat{\rho}}{\hat{\theta}}=1$ and

$$\left(\frac{\hat{\kappa}}{\hat{\epsilon}}-1\right)(\nu+\hat{\epsilon})<\zeta E_0\left(1-\frac{\hat{\rho}}{\hat{\theta}}\right),$$

which encompasses all of region A and a subset of region C in the current parameter regime. The region of parameter space corresponding to this condition for linear stability shares a boundary with (A.2) which bounds the region of existence of (iv) and is plotted in Figure 4.

Solution (iv) is stable for all values where it is feasible within the parameter space of Table 2, as illustrated in Figure 4. The bifurcations observed at the transitions between steady state regimes are all transcritical bifurcations.

C Parameter values

Parameter	Description	Value	Units	Reference
V_0	Reference VEGF concentration	8×10^{-3}	μM	50ng/ml used *in-vitro* (Matsushita et al., 2005) . Assumed 10 times larger for *in-vivo*.
A_0	Reference Ang1/2 concentration	8×10^{-3}	μM	80-500ng/ml used *in-vitro* (Audero et al., 2001), Assumed 10 times larger for *in-vivo*.
p_0	Reference PDGF concentration	8×10^{-3}	μM	Order of magnitude estimate from *in-vitro* experiments (Fox and DiCorletto, 1984).
E_0	Reference EC density	8×10^{-8}	μM	Using 10^5 receptors per cell gives relative EC density from *in-vitro* experiments.(Fiedler et al., 2004).
P_0	Reference PC density	4×10^{-8}	μM	Half reference EC density
ϕ	Average receptors per cell	10^5		Suggested by (Wang et al., 2002).
k^v_{on}	VEGF/VEGFR2 association	1.88×10^4	$\mu M^{-1} h^{-1}$	BIAcore experiments (Cunningham, 1999).
k^v_{off}	VEGF/VEGFR2 dissociation	0.99	h^{-1}	BIAcore experiments (Cunningham, 1999)
k^v_{int}	VEGF internalisation	0.86	h^{-1}	*In-vitro* experiments (Wang et al., 2002).
α_v	VEGF delivery	3×10^{-3}	$\mu M h^{-1}$	Fraction of reference value produced each hour from *in-vitro* experiments (Matsushita et al., 2005).
δ_v	VEGF decay	1	h^{-1}	Observed *in-vitro* (Serini et al., 2003)

Table C1: Default parameter set with units and references where applicable. Continued below

Parameter	Description	Value	Units	Reference
$k_{\text{on}}^{a_1}$	Ang1/Tie2 association	417	$\mu M^{-1}h^{-1}$	*In-vitro* from *kd* value (Maisonpierre, 1997)
$k_{\text{off}}^{a_1}$	Ang1/Tie2 dissociation	1.25	h^{-1}	*In-vitro* from *kd* value (Maisonpierre, 1997)
$k_{\text{int}}^{a_1}$	Ang1 internalisation	1	h^{-1}	*In-vitro* HUVECs: 70% of Ang1 internalised in one hour (Bogdanovic et al., 2006).
$k_{\text{on}}^{a_2}$	Ang2/Tie2 association	417	$\mu M^{-1}h^{-1}$	*In-vitro* from *kd* value (Maisonpierre, 1997)
$k_{\text{off}}^{a_2}$	Ang2/Tie2 dissociation	1.25	h^{-1}	*In-vitro* from *kd* value (Maisonpierre, 1997)
δ_{a_1}	Ang1 decay	4.69	h^{-1}	-
δ_{a_2}	Ang2 decay	0.0625	h^{-1}	-
δ_{a_w}	Intracellular Ang2 decay	0.031	h^{-1}	*In-vitro* subcellular Ang2 still visible after 15 hours (Fiedler et al., 2004).
α_{a_1}	Ang1 production	1×10^6	h^{-1}	-
α_{a_w}	Ang2 production	0.8	h^{-1}	-
α_{a_2}	Ang2 release	3	h^{-1}	*In-vitro* extracellular Ang2 reaches maximum after 20 minutes Fiedler et al. (2004).
α_p	PDGF Production	6.7×10^3	h^{-1}	Order of magnitude inferred from *in-vitro* experiments (Fox and DiCorletto, 1984).
k_{on}^{p}	PDGF/PDGFRbeta association	1.88×10^4	$\mu M^{-1}h^{-1}$	Assumed same as VEGF
k_{off}^{p}	PDGF/PDGFRbeta dissociation	0.86	h^{-1}	Used *kd* from *in-vitro* experiments (Fox and DiCorletto, 1984).
δ_p	PDGF decay	1.2	h^{-1}	-
θ	EC proliferation	0.0417	h^{-1}	Comparison of logistic growth curves for *in-vitro* EC proliferation (Milde et al., 2013).
ρ	EC death	0.02	h^{-1}	-
κ	PC proliferation	0.08	h^{-1}	*In-vitro* study of the growth of ECs and PCs (Prokopiou, 2013).
ϵ	PC death	0.04	h^{-1}	-
ζ	PC attachment	5×10^5	$\mu M^{-1}h^{-1}$	-
ν	PC detachment	5×10^{-3}	h^{-1}	-
η	maturity increase	0.01	h^{-1}	-
μ	maturity decrease	0.01	h^{-1}	-
c_{ep}	Threshold bound VEGF for EC proliferation	0.3	-	-
c_d	Threshold bound VEGF for EC death	0.1	-	-
c_a	Threshold bound Ang2 for EC proliferation	0.3	-	-
c_{pp}	Threshold bound PDGF for PC proliferation	0.02	-	-
λ	Ang2/Ang1 ratio for maturity decrease	8		

Table C1: Continued: Default parameter set with units and references where applicable.